Flow Enhancement of Tomographic Particle Image Velocimetry Measurements Using Sequential Data Assimilation

Chuangxin HE[1, 2](何创新), Peng WANG[1, 2](王鹏), Yingzheng LIU[1, 2]*(刘应征)
& Lian GAN[3](干联)

[1] *Key Laboratory of Education Ministry for Power Machinery and Engineering*
School of Mechanical Engineering, Shanghai Jiao Tong University
800 Dongchuan Road, Shanghai 200240, China

[2] *Gas Turbine Research Institute, Shanghai Jiao Tong University*
800 Dongchuan Road, Shanghai 200240, China

[3] *Department of Engineering, Durham University*
Durham DH1 3LE, UK

Manuscript revised in February 2022

* Corresponding author:
E-mail address: yzliu@sjtu.edu.cn (Y.Z. Liu)

Abstract

Sequential data assimilation (DA) was performed on three-dimensional flow fields of a circular jet measured by tomography particle image velocimetry (tomo-PIV). The work focused on the in-depth analysis of the flow enhancement and the pressure determination from volumetric flow measurement data. The jet was issued from a circular nozzle with an inner diameter of $D = 20$ mm. A split-screen configuration including two high-speed cameras was used to capture the particle images from four different views for the tomography reconstruction of the voxels in the tomo-PIV measurement. Planar PIV was also performed to obtain the benchmark two-dimensional velocity fields for validation. The adjoint-based sequential DA scheme was used with the measurement uncertainty implanted using a threshold function to recover the flow fields with high fidelity and fewer measurement errors. Pressure was determined by either the direct mode, with implementation directly in the DA solver, or by the separate mode, which included solving the Poisson equation on the DA-recovered flow fields. Sequential DA recovered high signal-to-noise flow fields that had piecewise-smooth temporal variations due to the intermittent constraints of the observations, while only the temporal sequence of the fields at the observational instances was selected as the DA output. Errors were significantly reduced, and DA improved the divergence condition of the three-dimensional flow fields. DA also enhanced the dynamical features of the vortical structures, and the pressure determined by both modes successfully captured the downstream convection signatures of the vortex rings.

Keywords: Sequential data assimilation, tomo-PIV, flow enhancement, pressure determination, jet flow

1. Introduction

With the rapid development of computer science and measurement technologies, the acquisition of turbulent flow data has been developed to encompass full three-dimensional schemes including magnetic resonance imaging[1] and volumetric particle image velocimetry (V-PIV)[2]. Tomographic PIV (tomo-PIV)[3] is one of the most widely used V-PIV techniques for three-dimensional three-component (3D3C) flow field acquisition due to its relatively large measurement volume and high spatial resolution. Tomo-PIV uses multiple cameras to capture particle images from different angles of view, which are then used for the tomographic reconstruction of three-dimensional voxels. The tomo-PIV measurement is known to be affected by calibration errors, cross-correlation errors and ghost particles induced by the tomographic reconstruction procedure. These effects consequently result in large uncertainty in the flow field acquisition and subsequently in the pressure field determination, suggesting the importance of error reduction for measurement data in experimental fluid research. “Flow enhancement” is defined in this work following data enhancement[4], to denote the reduction of the measurement errors in flow field data and the inversion of the pressure field.

Tomo-PIV has been established for use in the reconstruction of three-dimensional arrays of light intensity that are discretised over voxels using, usually, a multiplicative algebraic reconstruction technique (MART) algorithm. The 3D3C velocity vectors are then determined by cross-correlating two successive tomograms[3, 5]. While the reconstruction mainly relies on a precursor calibration, the mapping function of the coordinates from the physical space to the image space can be erroneous due to either inaccurate calibration plates or mathematical issues[6]. Another issue in the tomographic reconstruction is the existence of ghost particles formed at the intersection of the lines of sight where particles are simultaneously present[7]. This effect has been reported to be the dominant source of measurement error for high sending density[8] in tomo-PIV measurements and is the main way this technique differs from two-dimensional PIV techniques. Regarding the above-mentioned measurement errors, numerous studies have sought to enhance the flow field to a specific performance, including self-calibration to reduce reconstruction error[6] and using a motion tracking enhancement algorithm to remove the ghost particles[9]. The most recent development on Lagrangian particle tracking (LPT), i.e., Shake-the-Box (STB), enables the tracking of individual tracer particles typically following a flow in a three-dimensional volume [10]. Cross-correlation error and the effect of the ghost particles are substantially reduced. However, considerable uncertainties still exist in the flow fields as errors in reconstruction and vector determination cannot be completely eliminated in either tomo-PIV or LPT measurements. The most notable feature of these methods is the divergence-free error that occurs from the loss of physical constraints in the calculation of image processing in the measurements. This loss inevitably causes difficulties in the analysis of turbulence dynamics and pressure computations. Wang et al.[11] proposed a divergence-free smoothing method based on the combination of penalised least squares regression and the divergence corrective scheme. In this method, truncation exists for small-scale flow structures due to the low-pass filtering effect of the smoothing operation.

Another motivation of the present flow enhancement is the determination of the pressure field, which is difficult to measure directly inside the fluid domain[12, 13]. As mentioned previously, the pressure field is generally calculated from a time sequence of PIV data by either gradient integration or solving the Poisson equation[14, 15]. Due to the three-dimensional nature of turbulent flows, 3D3C flow data are usually required[12, 16] for flows in which the contribution of the third component is significant. Applications of the pressure determination from three-dimensional velocity data have been realised. These include the flow of a flapping wing determined from a scanning PIV measurement[17], the turbulent boundary layer measured by single-snapshot tomo-PIV[18], and a vortex ring measured by LPT in which the Lagrangian acceleration was evaluated[19]. However, boundary condition effects and error accumulation in both the gradient integration and Poisson equation methods are important due to limitations of the PIV field of view and measurement noise[20, 21]. The pressure and pressure gradient are thus difficult to determined due to the turbulence which is of similar level with the large-scale organised patterns in the flow; large-region PIV measurements in which the pressure, or its gradients, at the boundaries can be easily determined is also required.

Data assimilation (DA) is a technique that fuses experimental measurements with numerical simulations to gather observations (measurement data) at a given time and use flow dynamic equations to estimate future states (e.g., global flow data)[22]. This technique has been applied in turbulent flow[23-25]. While the statistic-based DA method uses complicated data computations[26-28], adjoint-based DA has become popular for use with flow recovery. The adjoint equation system, including the corresponding boundary conditions, is derived and solved together with the primary equation system[29-32]. The time-averaged flow and pressured fields can thus be accurately determined within the constraints of relatively temporally-sparse local measurement data. This approach is methodologically similar to the least square method[33, 34] which use the measured data as a constraint to force the calculated results approach the prior predictions. However, DA utilises the measured flow data to optimise the momentum predictor and thus determine firstly the flow filed which obeys the fluid governing equations before the pressure field can be readily obtained. It benefits from the predictive ability of numerical simulation models while the local measurement data such as the off-plane component are absent, and large uncertainties or measurement noise are contained. Using the adjoint formulation, a four-dimensional variational method (4DVar) has been developed for unsteady flow assimilation and instantaneous pressure determination[35, 36]. However, integration in 4DVar must be performed forward for the primary equations and backward for the adjoint equations. This necessitates saving the data at all time steps[37], which results in huge storage space requirements and slow processing speeds. Our previous work developed an adjoint-based sequential DA scheme that did not need backward integration, which was successfully applied to the determination of unsteady pressure in a synthetic circular jet flow[21] and a blunt plate[38]. Accordingly, there is great potential for flow enhancement and pressure determination using sequential DA in turbulent flows measured by tomo-PIV.

The present work applied the adjoint-based sequential DA on three-dimensional flow fields measured by tomo-PIV. While our previous efforts[21] were mainly concentrated on the pressure determination based on the relatively accurate flow fields obtained by numerical simulation, the present implementation involved a threshold function to cope with the significant uncertainty in large-domain tomo-PIV measurements. The circular jet was used as the benchmark, as it had been widely used for the assessment for volumetric flow measurements, and had significant variation of the flow in the depth direction. The Reynolds number based on the nozzle diameter D and the bulk velocity at the jet nozzle exit U_0 was $Re = 3{,}000$, at which the flow was featured by the convection of large-scale vortex rings due to the Kelvin–Helmholtz instability followed by the vortex breakdown. The tomo-PIV measurement was performed to acquire the 3D3C flow field in the jet initial region and was used as observations for the DA process. The present measurement domain was considerably large for tomo-PIV measurement. It is worth noting that this measurement size in the depth direction was much larger than that in our previous experiment[21], which inevitably induced significant particle overlap in camera images and produced ghost particles, thus higher level of measurement errors. The present work is strongly motivated to utilise and assess the DA scheme on the flow field improvement for noisy tomo-PIV results. A planar-PIV measurement was also conducted for comparison. The measurement uncertainty of tomo-PIV was evaluated using the mean flow field of the planar-PIV data and input into the DA equations for the flow enhancement. Details of the flow and pressure evolutions were analysed to gain a better understanding of the DA performance.

2. Mathematics Fundamentals

2.1 Sequential DA scheme

The present formulation is based on our previous derivation[21] but with measurement uncertainty included to promote the flow field enhancement. For incompressible flows, a forcing term $\boldsymbol{F}$ is added to the time-dependent Navier-Stokes (N-S) equations and is optimised to minimise the discrepancy between the observational data (tomo-PIV measurement) and predictions. This yields

$$\frac{\partial \boldsymbol{U}}{\partial t} + (\boldsymbol{U} \cdot \nabla)\boldsymbol{U} = -\nabla p + \nu \nabla^2 \boldsymbol{U} + \boldsymbol{F} \tag{1}$$

$$\nabla \cdot \boldsymbol{U} = 0 \tag{2}$$

where ν is the kinematic viscosity of the fluid and p denotes the pressure divided by the fluid density. The DA technique can be achieved by minimising the cost function $\mathcal{J}$ subject to the governing equations using an optimised distribution of $\boldsymbol{F}$. This is expressed as

$$\begin{gathered}\text{minimise } \mathcal{J} = \xi \int_{t_0}^{t_0+\Delta t} \int_{\Omega} \sum_i \left[M f_{\varepsilon,i} \left(\frac{U_i - U_{\text{tomo},i}}{U_0} \right)^2 \right] \mathrm{d}\Omega \mathrm{d}t, \\ \text{subject to } \mathcal{R}(\boldsymbol{U}, p, \boldsymbol{F}) = 0. \end{gathered} \tag{3}$$

where t_0 and Δt are the initial time and the time step of the computation, respectively. Ω represents the computational domain. A weighting function M is defined to specify the region where the observational data are obtained. ξ is a dimension converter of dimensions $[\mathrm{L}^2 \cdot \mathrm{T}^{-3}]$ with a value of unity, to cope with the dimensional inconsistency. U_0 denotes the free-stream or the inflow bulk velocity. $\mathcal{R}(\boldsymbol{U}, p, \boldsymbol{F})$ includes the incompressible unsteady N-S equations and the continuity equation. Different from our previous implementation[21], a threshold function associated with the measurement uncertainty $\boldsymbol{f}_\varepsilon$ is used in the cost function to consider the measurement error in the observations. The three components $f_{\varepsilon,x}, f_{\varepsilon,y}$ and $f_{\varepsilon,z}$ denote the *x*, *y* and *z* components, respectively. The threshold function is defined as

$$f_{\varepsilon,i} = \tanh \left[\left(\frac{\overline{U}_i - \overline{U}_{\text{tomo},i}}{\varepsilon_i} \right)^{20} \right], (i = x, y, z) \tag{4}$$

where, '‾' denotes the time average. The exponent 20 is used to force a rapid switching of the threshold function between 0 and 1; it is noted that this value has trivial effect on the final results once it is large enough. The ε_i parameter is the tomo-PIV measurement uncertainty, which is defined by the difference between the mean velocity fields of tomo-PIV and planar-PIV measurements, i.e.,

$$\varepsilon_i = \left| \overline{U}_{\text{tomo},i} - \overline{U}_{\text{planar},i} \right|, (i = x, y, z) \tag{5}$$

Due to the different dimensions and spatial resolution of the planar- and tomo-PIV results, the planar-PIV measurement results should be duplicated azimuthally and interpolated onto the three-dimensional mesh before subtracting the tomo-PIV results. The threshold function specifies a criterion for how close the predicted flow should be to the observation. $f_{\varepsilon,i}$ approaches zero in regions where the discrepancy between the predicted flow and the observation becomes smaller than the measurement uncertainty ε_i. Thus, a high level of measurement error is likely to be removed by introducing more confidence into the model prediction. The measurement uncertainty ε_i plays an important role in the error removal and flow enhancement of the tomo-PIV measurements. However, the definition of this uncertainty is tricky due to the complexity of mapping the camera images to the three-dimensional vector fields. The present definition in terms of mean flows using the planar-PIV results, which are usually of much smaller uncertainty once the measurements are carefully performed, as the reference performs reasonably well, with only minor defects. It is important to note that more precise uncertainty assessment method should be developed for more complex flow configurations.

We obtain a constraint optimisation problem that can be solved by introducing a Lagrange function $\mathcal{L}$ such that

$$\mathcal{L} = \mathcal{J} + \int_{t_0}^{t_0+\Delta t} \int_{\Omega} (\boldsymbol{V}, q)\boldsymbol{\mathcal{R}}\mathrm{d}\Omega\mathrm{d}t, \tag{6}$$

where $\boldsymbol{V}$ and q denote the adjoint velocity and adjoint pressure introduced as the Lagrange multipliers. $\boldsymbol{\mathcal{R}}$ includes the N-S and continuous equations. The inner product between $(\boldsymbol{V}, q)$ and $\boldsymbol{\mathcal{R}}$ produces a scalar denoting the constraint of the governing equations. After obtaining the sensitivities of the Lagrange function $\mathcal{L}$ with respect to $\boldsymbol{F}$ by setting the variations of $\mathcal{L}$ with respect to other state variables to zero, the optimal $\boldsymbol{F}$ distribution can be determined. Accordingly, the adjoint equations associated with the adjoint state variables $\boldsymbol{V}$ and q are

$$\frac{\boldsymbol{V}}{\Delta t} + \nabla\boldsymbol{U}\cdot\boldsymbol{V} - (\boldsymbol{U}\cdot\nabla)\boldsymbol{V} - \nu\nabla^2\boldsymbol{V} + \nabla q + 2\xi M\left(\boldsymbol{f}_\varepsilon \circ \frac{\boldsymbol{U} - \boldsymbol{U}_{\mathrm{tomo}}}{U_0^2}\right) = 0 \tag{7}$$

$$\nabla\cdot\boldsymbol{V} = 0 \tag{8}$$

with $\nabla\boldsymbol{U}\cdot\boldsymbol{V} = V_j\frac{\partial U_j}{\partial x_i}$. The operator '$\circ$' denotes the Hadamard product. For the inflow, wall and far-field boundaries where the primary state variable $\boldsymbol{U}$ is specified, the boundary conditions are

$$V_\tau = 0, \qquad V_n = 0 \tag{9}$$

$$\boldsymbol{n}\cdot\nabla q = 0 \tag{10}$$

For the outflow boundaries where the zero-gradient condition is used for the primary state variables

$\boldsymbol{U}$, the conditions are

$$U_n \cdot V_\tau + \nu(\boldsymbol{n} \cdot \nabla)U_\tau = 0 \tag{11}$$

$$U_n \cdot V_n + \nu(\boldsymbol{n} \cdot \nabla)U_n - q = 0 \tag{12}$$

where the subscripts n and τ denote the normal and tangential components of the variables, respectively. $\boldsymbol{n}$ is the unit normal vector at the boundaries. Detailed derivation of the adjoint equations and boundary conditions was according to[39].

Once the adjoint state variables are obtained, the sensitivities of the Lagrange function $\mathcal{L}$ with respect to the forcing $\boldsymbol{F}$ can be computed according to

$$\frac{\partial \mathcal{L}}{\partial \boldsymbol{F}} = -\boldsymbol{V} \tag{13}$$

As the sensitivity with respect to the state variables is forced to disappear, the forcing function $\boldsymbol{F}$ can be adjusted gradually according to Eq. (14) using the steepest descent algorithm [40] to minimise the cost function.

$$\boldsymbol{F} = \boldsymbol{F} - \lambda \frac{\partial \mathcal{L}}{\partial \boldsymbol{F}} \tag{15}$$

where λ is the step length estimated according to $\lambda = (0.01\sim0.1)/(\partial \mathcal{L}/\partial \boldsymbol{F})_{\max}$. Note that the small value of λ is beneficial to the numerical stability but slows down the convergence. An appropriate λ value can be easily obtained in the computation of the first few time steps.

Fig. 1 shows the iterative procedure to achieve the sequential DA. The biggest difference from the conventional 4DVar algorithm is that the present DA scheme integrates all the way forward in time. The judgement of whether the observations are present is made at each time step to realise the conventional numerical simulation when observations are absent. At a time step when observations are present, the adjoint equations are solved with the updated $\boldsymbol{F}$ and the iteration condition, such that the maximum number of iterative loops or the residual is assessed. The computation moves on to the next time step when the iteration condition is met. Note also that as the time interval between the observations is usually larger than the time step of the computation, the flow has an abrupt switching to the time step when observations are present from the previous time steps (will be shown in Fig. 10), exhibiting behaviour typical of sequential DA with a piecewise-smooth flow variation in time. Therefore, only the flow data at time steps when observations are present are selected as the DA results.

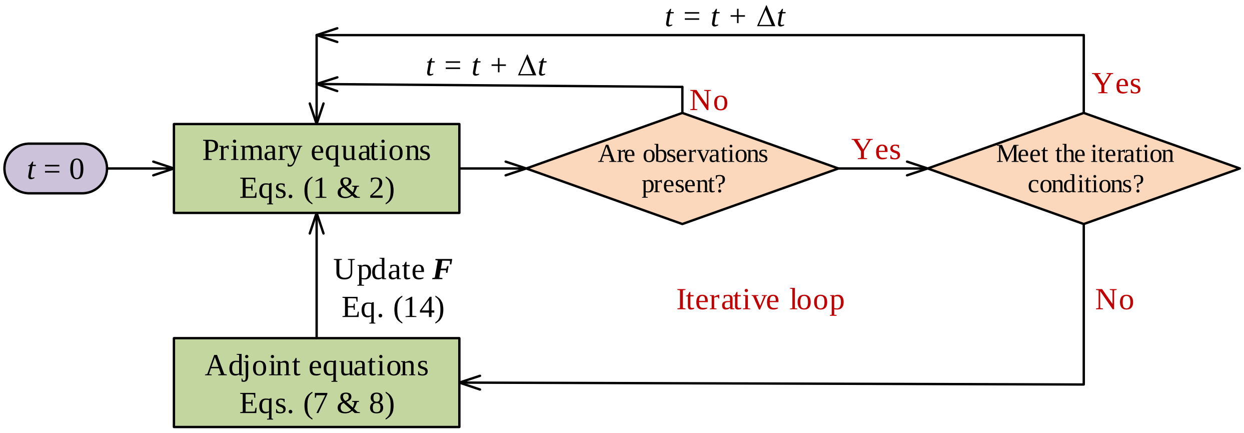
$t = t + \Delta t$
$t = t + \Delta t$
No
Yes
Yes
$t = 0$
Primary equations
Eqs. (1 & 2)
Are observations present?
Meet the iteration conditions?
Update $\boldsymbol{F}$
Eq. (14)
Iterative loop
No
Adjoint equations
Eqs. (7 & 8)

Fig. 1 Iterative procedure of the primary-adjoint system.

2.2 Pressure determination scheme

In the framework of conventional unsteady flow simulation, the pressure implicit splitting of operators (PISO) algorithm is used to solve the N-S and the continuity equations. The semi-discretised form of the N-S equations[41] is

$$a_P \boldsymbol{U}_P = \boldsymbol{H}(\boldsymbol{U}) - \nabla p. \tag{16}$$

where a_P is the matrix coefficients for the implicit velocities. The $\boldsymbol{H}(\boldsymbol{U})$ term consists of the matrix coefficients for all neighbours multiplied by the corresponding velocities, the source part of the transient term and all other source terms except the pressure gradient. The pressure is computed after solving the N-S equations using a Poisson equation derived from the flow mass conservation,

$$\nabla \cdot \left(\frac{1}{a_P} \nabla p \right) = \sum_f S \cdot \left[\frac{\boldsymbol{H}(\boldsymbol{U})}{a_P} \right]_f \tag{17}$$

where the subscript “f” denotes the mesh surface, and S is the surface area. At each iterative loop, the N-S equations and Poisson equation are solved, and the flow velocity and pressure are updated. In the present primary-adjoint system, however, the pressure finally converges to a distribution subject to the forcing, as $\boldsymbol{F}$ is contained in the $\boldsymbol{H}(\boldsymbol{U})$ term. To obtain a pressure with the converged velocity field as if the flow develops naturally, the contribution of $\boldsymbol{F}$ in Eq. (16) needs to be excluded. This gives

$$\nabla \cdot \left(\frac{1}{a_P} \nabla p\right) = \sum_f S \cdot \left[\frac{\boldsymbol{H}(\boldsymbol{U}) + \boldsymbol{F}}{a_P}\right]_f \tag{18}$$

after the final iterative loop to compute the pressure distribution. Eq. (17) can be solved via coupling into the primary-adjoint system. The $\boldsymbol{H}(\boldsymbol{U})$ term contains the difference between the flow fields at the observational instance and those at the previous time step. The abrupt switching of the flow induces specific errors in the pressure determination. Here, two pressure fields are saved: the forced pressure with the contribution of $\boldsymbol{F}$ computed by Eq. (16) to realise the velocity-pressure coupling loop and the natural pressure excluding the $\boldsymbol{F}$ contribution computed by Eq. (17). We call the determination method of the natural pressure the 'direct mode'. Both pressures also have piecewise-smooth variations in time while the natural pressure data at the instances of observation are selected as the DA results.

The pressure can also be computed separately using the DA flow fields at each observational instance. This method is named 'separate mode' in this study. The time interval is much larger than the computational time step and thus also induces error in the calculation of the velocity time derivative. This approach is similar to the pressure determination from PIV measurements by solving the Poisson equation. Currently, the flow fields are obtained by DA with less measurement and divergence errors and in larger domains. This results in the pressure computation being less sensitive to the boundary conditions and flow errors.

3. Experimental and Numerical Setups

3.1 Experimental setup

The experiment was conducted in an octagonal tank (sidewall width, 250 mm; height, 900 mm) that was previously used in[42] and is shown in Fig. 2a. An overflow chamber was designed to control the free surface location and feed the jet flow with the assistance of a frequency-converter pump. A nozzle with a contraction ratio of 2:1 and an exit diameter of $D = 20$ mm was installed at the bottom of the octagonal tank. The exit was 200 mm above the bottom surface to minimise the wall effect on the flow field. The jet fluid first entered a flow stabiliser located below the bottom surface of the octagonal tank. This stabiliser incorporated a cylindrical filter to change the flow direction uniformly from upward to radial and a honeycomb filter with a diameter of $2D$ to dampen the large-scale structure and crosswise velocity upstream of the nozzle. The Reynolds number was fixed at $Re = 3{,}000$ which was defined based on the bulk velocity U_0 $(0.135\mathrm{m/s})$ in the nozzle and the nozzle exit equivalent diameter D.

The three-dimensional flow-field downstream of the nozzle exit was measured via tomo-PIV. The global seeding of the complete tank was realised with 50-µm polyamide particles (Dantec, Denmark). A 25 W continuous-wave laser at 532 nm (Millennia EV25S, USA) was used for the illumination. The laser included a compacted combination of cylindrical lenses to produce a 50-mm-diameter light column through the jet centreline and also had a surface chamber to eliminate the free surface effects on the illumination. Particle images were captured using two 12-bit complementary metal-oxide semiconductor (CMOS) cameras (PCO, Germany) with a spatial resolution of 2,000 × 2,000 pixels and lenses (Laowa 100mm/F2.8, China) with an aperture value of F11. The images were taken using a double-exposure mode controlled by the synchroniser, i.e., with a sampling rate of 100 image pairs per second and a time interval of 2 ms between the frames in each image pair. These parameters yielded a particle shift of approximately 6 pixels in the main region. The particle size was around 4 × 4 pixels with a density of approximately 0.02 Nppp (number of particles per pixel). The exposure time for each image was fixed at 1 ms. Using an appropriate combination of prismatic and planar mirrors[43], each camera was split into two views, as shown by the yellow dashed line in Fig. 2a. This resulted in four different views along the radial direction with an approximately 30° azimuthal angle increment and a field of view of 1,000 × 2,000 pixels. This configuration reduced the number of cameras required but maintained an equivalent removal of ghost particles with the four-camera system. Due to the resolution decrease of each image caused by the screen splitting, an appropriate layout needs to be designed to keep necessary pixels in the jet region, and care must be taken to avoid cross-talk among the particle images from two sides of the split screen. For comparison, the planar-PIV measurement was also conducted on the longitudinal plane by modulating the laser column to a sheet of 1 mm in thickness. Only one camera was used, without the split-screen configuration. Other configurations of the laser and camera remained identical to those used for the tomo-PIV measurements.

The camera calibration, together with volume self-calibration[6], was performed using a dotted-array plane with a dot diameter of 1.5 mm and a distance of 10 mm. Three-dimensional calibration was achieved by a 30-mm normal shift of the calibration plate controlled by a traverse mechanism. The velocity vectors were calculated from the raw particle volumes using a TOMOpro code developed in-house[44, 45]. In the tomo-PIV measurement, the size of the reconstructed volume was 100 mm ($5D$ in x direction) × 50 mm ($2.5D$ in y direction) × 50 mm ($2.5D$ in z direction) centred at the nozzle axis, as shown in Fig. 2b. Image preprocessing was applied to remove noise and improve the volume reconstructions. A global view of the particle image and a close-up view are shown in Fig. 3. The original particles in the image are irregularly shaped, with a very dense sparsity ratio, resulting in an excessive computational cost of each MART iteration. Before background subtraction and local normalisation, the images were first bandpass filtered in the image processing. This iteration gave rise to well-shaped particles and a high sparsity ratio with clear space between particles. The MART technique was used to reconstruct the three-dimensional distribution of the particle grayscale with a resolution of 11 voxels/mm, resulting in a particle sparsity of approximately 1.5% for the whole reconstructed domain. The sub-voxel accuracy PIV algorithm was based on the iterative multigrid volumetric cross-correlation approach with a final pass (minimum) interrogation volume size of $32 \times 32 \times 32$ voxels (physical size of 2.86 mm^3) and 50% overlap. This yielded a resolution of 14 vectors per nozzle diameter D. A total of 600 flow-field snapshots were captured, spanning approximately 18 passing loops of the large-scale vortex rings according to the Strouhal number $St =$ 0.4. The planar-PIV measurement used an interrogation window size of 32×32 pixels (physical size of 2 mm^3), and a 50% overlap yielded a vector resolution of 20 vectors across the nozzle diameter D. A total of 3,000 two-dimensional flow-field snapshots were obtained for analysis.

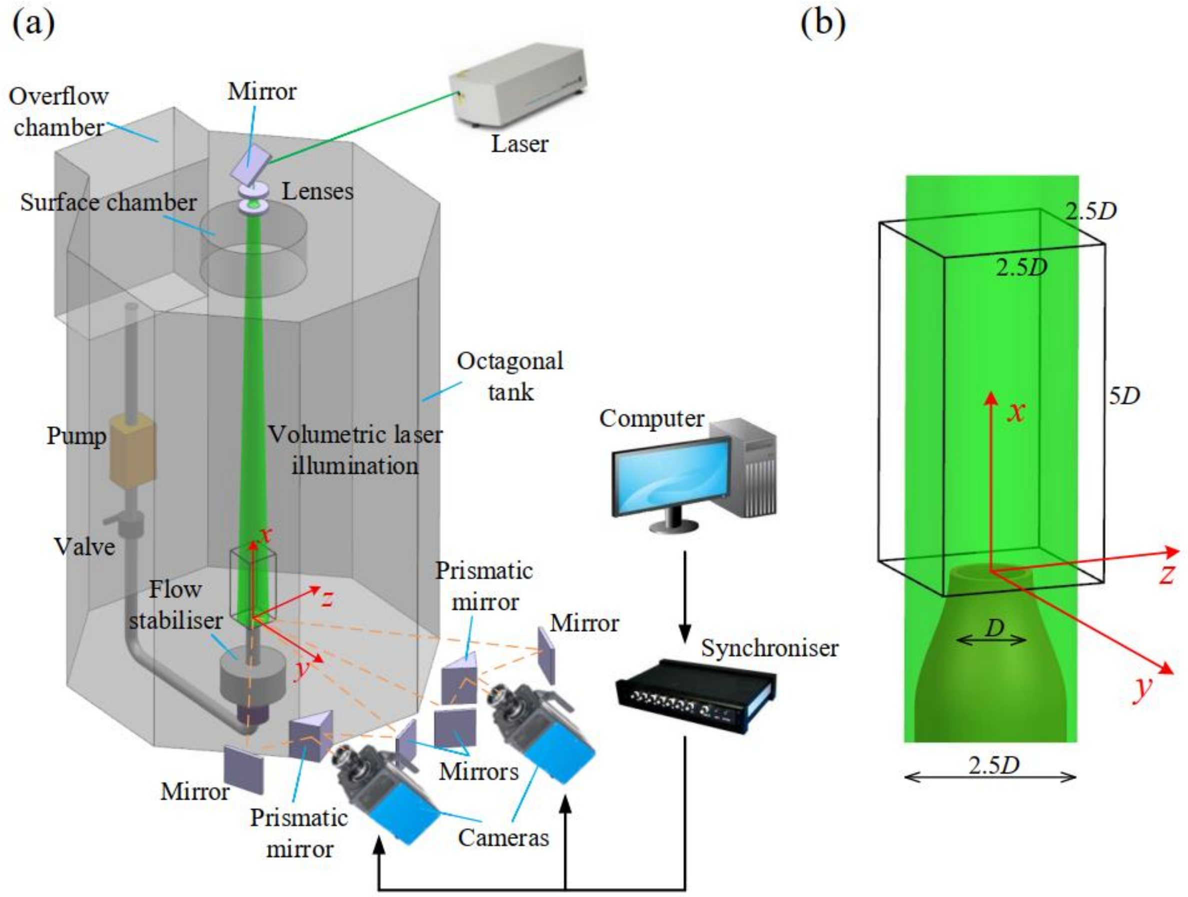
(a)
Overflow chamber
Mirror
Laser
Lenses
Surface chamber
Octagonal tank
Pump
Volumetric laser illumination
Computer
Valve
x
Flow stabiliser
z
y
Prismatic mirror
Mirror
Synchroniser
Mirrors
Mirror
Prismatic mirror
Cameras
(b)
2.5D
2.5D
5D
x
z
D
y
2.5D

Fig. 2 Schematic diagram of the tomo-PIV setup: (a) instruments layout; (b) the reconstruction domain.

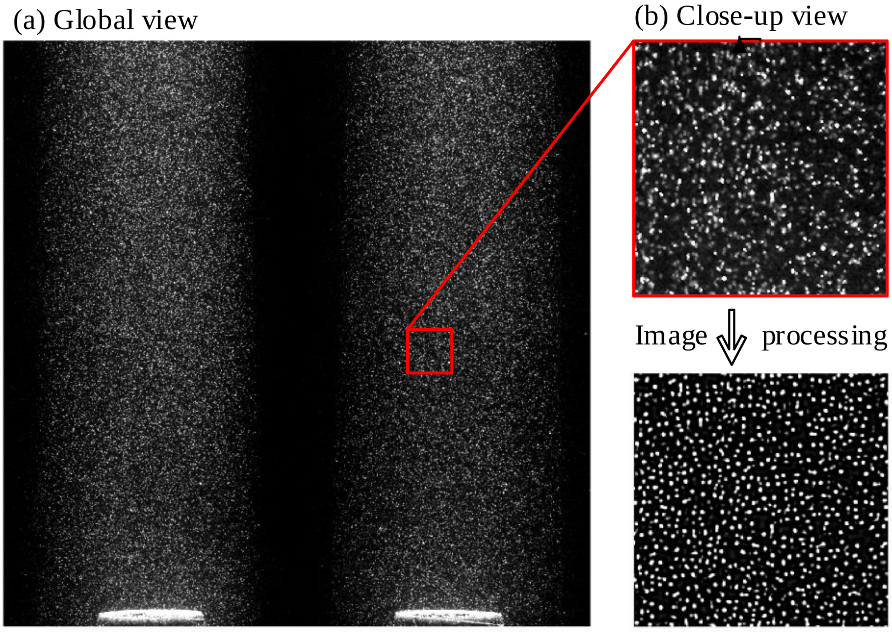

Fig. 3 Particle image captured by the split-screen camera: (a) the global view; (b) the close-up review of the original and the processed particle images.

3.2 Computational setup

DA was performed in a three-dimensional domain, as shown in Fig. 4a. The domain had a length of $32D$ and diameter $30D$ (where D is the nozzle diameter) to eliminate the boundary effects on the main stream. Previous work[46] showed that the jet spread only about $10D$ in the radial direction at the domain exit, indicating that the domain size of $30D$ was sufficient for the present computations. It is important to note that such large computational domain is not required for internal flows, as physical domain size and boundary conditions can be directly applied. The inlet boundary extended $1D$ upstream of the nozzle exit to reduce the inflow boundary effects on the flow. A structured O-type mesh was used as the base mesh as shown in Fig. 4b. The azimuthal direction was discretised uniformly using 64 mesh elements. The mesh size was gradually increased in the radial direction to reduce the computational cost but keep a fine resolution where necessary. One level of mesh refinement technique was performed to increase the resolution in the jet region, resulting in approximately 1.2 million nodes.

In the DA process, the tomo-PIV measurements were used as the observational data located in the region with ranges of $0.1 \leq x/D \leq 5$ and $-1.25 \leq r/D \leq 1.25$ $(r = \sqrt{y^2 + z^2})$ as shown in Fig. 4a. The time sequence of the tomo-PIV data was interpolated onto the computational mesh in the observational region with a time interval of $\Delta T = 0.01$ s, as shown in Fig. 4b. A mean distribution of the streamwise velocity according to the planar-PIV measurement and the fluctuating part extracted from the fully developed turbulent channel flow were superimposed onto the inflow boundary for the boundary conditions of the primary variables. The zero-gradient and free-slip conditions for the primary velocity were imposed on the outflow and far-field boundaries, respectively. The velocity on the co-flow boundary was $0.01U_0$, which was small enough to void the effects on the main flow while also being beneficial for the numerical stability. The pressure on the outflow boundary was specified to be zero, while a zero-gradient condition was imposed on other boundaries. All of the boundary conditions for the adjoint variables were specified according to Section 2.1. Both the primary and adjoint equations were discretised using the second-order scheme, which includes staggering characteristics and the introduction of small amounts of upwind to remove unphysical fluctuations. In the DA computation, the primary velocity was initialised from a precursor simulation result using the laminar model and the superimposed primary inflow condition. The time step used in the DA computation was $\Delta t = 0.002$ s and the observational data were implanted every 5 time steps. $\lambda = 10^4$ was used in Eq. (14), and the number of the iterative loop was fixed at 20 (Fig. 6), which yielded good stability and a reasonable convergence for both the velocity assimilation and pressure determination. The computation was performed using the open-source code OpenFOAM. Only the primary equations were solved with $\boldsymbol{F} = 0$ once the observations were absent.

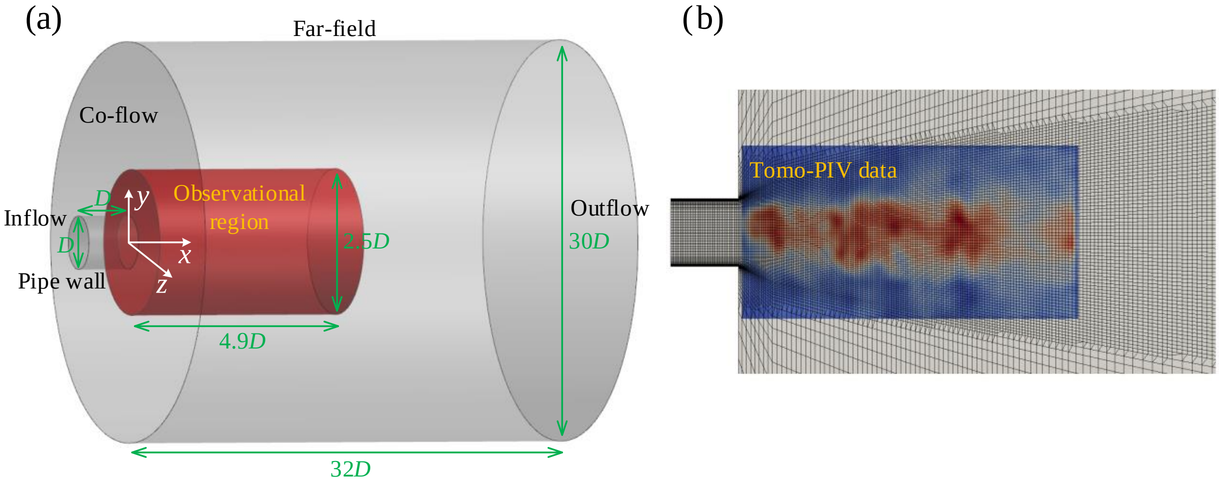

Fig. 4 Schematic diagram of the DA setup: (a) the computational domain; (b) the mesh implanted with the tomo-PIV data.

In the DA computation, a weighting function M was defined to represent the relative importance of the observations in different regions, i.e., lower degree of confidence on the observational data was imposed in the region with smaller M. As shown in Fig. 5a, M was defined as the normalised streamwise velocity fields of the planar-PIV measurement. These fields were interpolated azimuthally to a three-dimensional computational domain, with a linear attenuation to zero in the region of $0 < x/D < 1$ to reconcile the effect of the disparity in the inflow boundary conditions between the DA and the tomo-PIV data. This weighting function was beneficial for the smooth transition of the flow from the nozzle to the jet region where the flow was constrained by the observations, and for the noise elimination in the side regions where the flow velocity was significantly smaller than that in the main stream. However, the weighting function does not make much sense for the assimilated results once the residual, i.e., the difference between the predictions and the observations, becomes significantly small within the iteration. This weighting function is thus coupled with the threshold function to loosen the observational constraint where large uncertainty exists in the tomo-PIV data. To define the tomo-PIV uncertainty, the planar-PIV measurement results were first interpolated onto the three-dimensional computational mesh before subtracting the tomo-PIV results. The tomo-PIV uncertainty is defined in Eq. (5) and was normalised using the jet inflow velocity U_0 in Fig. 5(b-d), where the three components are shown.

Large uncertainty existed in the initial shear layer of the jet except for the z-component of the velocity. Specifically, large uncertainty occurred for ε_x in the negative region of the y coordinate in Fig. 5b (large distance from the camera in the depth direction). It was more significant for ε_y in the whole measurement region due to ghost particles in the tomographic reconstruction, which thus created large measurement uncertainty for the velocity component in the depth direction. The velocity component parallel to the camera layout in tomo-PIV measurement agreed well with the planar-PIV results, which yielded quite small uncertainty, as shown in Fig. 5d.

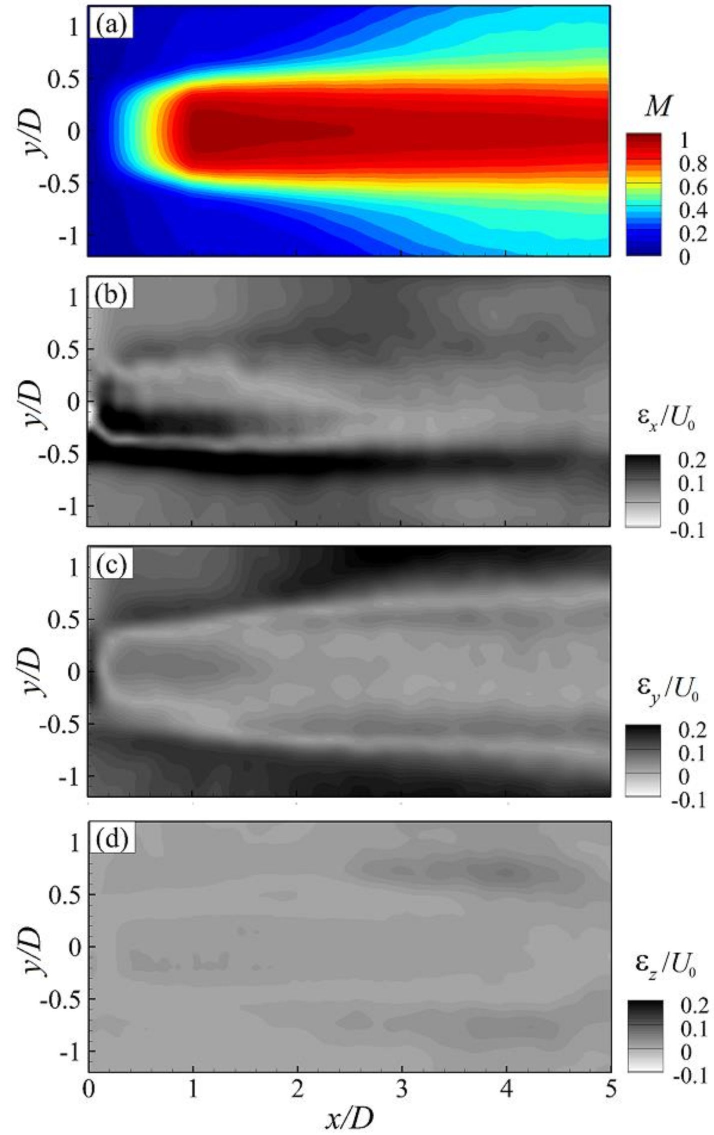

Fig. 5 Distributions of the weighting function and measurement error: (a) the weighting function M; (b-d) and different components of the error.

The tomo-PIV measurement uncertainty shown in Fig. 5(b-d) is only a rough definition in terms of the mean flow distribution. Indeed, the uncertainty for each flow snapshot was much more complicated than the present definition. For a well-configured two-dimensional PIV system, the uncertainty comes mainly from the image matching for vector determination [47, 48], which is associated with the displacement gradient of a particle, the off-plane motion, the seeding density and background noise. However, the tomo-PIV measurement has an additional source of uncertainty in the particle tomographic reconstruction, including the calibration error and effects of the ghost particles. This uncertainty source has been observed to be dominant compared to that of image matching, but it is difficult to evaluate. The present uncertainty distribution was inappropriate in the region where ε_i approached zero, but the instantaneous field of the tomo-PIV measurement contained considerable error, which usually causes computational difficulties in reducing the residual further to a certain level. Fig. 6a demonstrates the variation in the domain-averaged threshold function $\langle \boldsymbol{f}_{\varepsilon} \rangle$ with respect to the iterative loop number in a selected time step and using a step length $\lambda = 10^4$. This value directly reflects the DA residual that represented the discrepancy between the observations and the predictions. $\langle \boldsymbol{f}_{\varepsilon} \rangle$ decreased rapidly in the beginning for each component but remained at a certain level for the iterative loop $n_i > 20$ with a slowly decreasing rate. The $\langle f_{\varepsilon,z} \rangle$ was much larger than the other two components due to the low measurement uncertainty, as shown in Fig. 5d, and the relatively large computational residual (Fig. 6d). According to Fig. 6a, the number of iterative loops was fixed at $n_i = 20$ for the primary-adjoint system with $\lambda = 10^4$. The other λ values were tested for convergence, and the optimal n_i was also changed. However, they had little effect on the final results but did affect the variation in the computational efforts. Fig. 6(b-d) shows the threshold function distribution at $n_i = 20$ on the jet centre plane, illustrating that the assimilated flow in the observational region had not approached the tomo-PIV measurement within the defined uncertainty level. Nevertheless, the residual was helpful for reducing noise in tomo-PIV measurement.

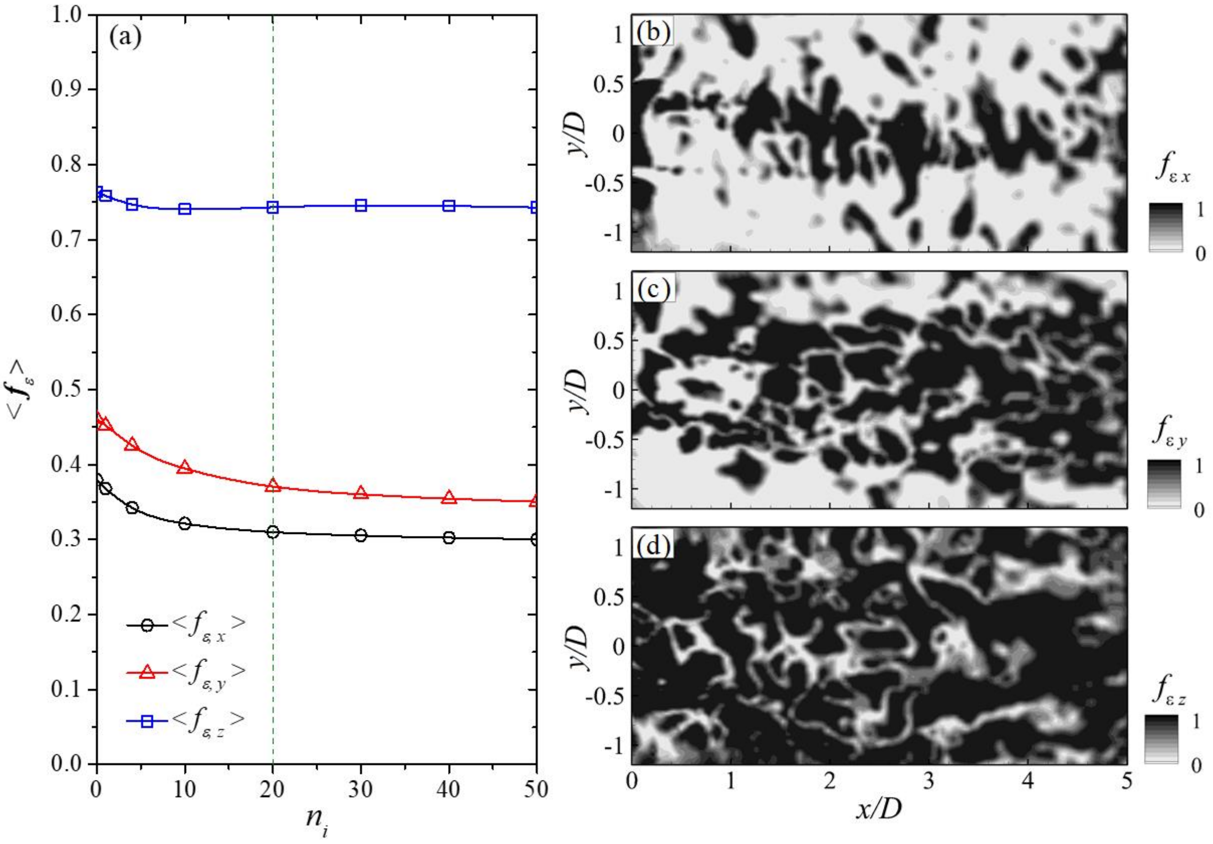

Fig. 6 Convergence of the iteration: (a) residual decay with respect to the iteration loops; (b-d) distributions of the threshold functions at $n_i = 20$.

4. Results and discussion

4.1 Overview of the DA results

The flow snapshots in Fig. 7 present an overview of the PIV measurements and the DA results at a large time when the flow is well developed. As the superimposed inflow condition was used in the DA, the flow inside the nozzle section exhibited typical features of a developed pipe flow with a smooth transition to the main jet flow outside the nozzle. Note that the dashed white box indicates the observational region and the observational tomo-PIV results are shown in the solid red box. An important feature of the tomo-PIV measurement and the DA result is the similarity of the flow distributions in the large-scale pattern. There was more error contained in the tomo-PIV measurement, as shown by the discontinuity of the flow contours. This difference demonstrates that the DA procedure can remove errors using the N-S equations as a filter. As the flow in the observational region is assimilated, a consistent development of the flow in the downstream region was observed. The observations facilitated flow recovery inside the observational region and downstream flow due to the spatial correlation. The planar-PIV measurement result is also shown in Fig. 7 for comparison. Although the planar-PIV measurement was not performed simultaneously with tomo-PIV, the general large-scale pattern of the fluid puffs (induced by the vortex rings) was confirmed except for the notable measurement noise in the instantaneous field. These planar-PIV data were used further for quantitative validation of DA.

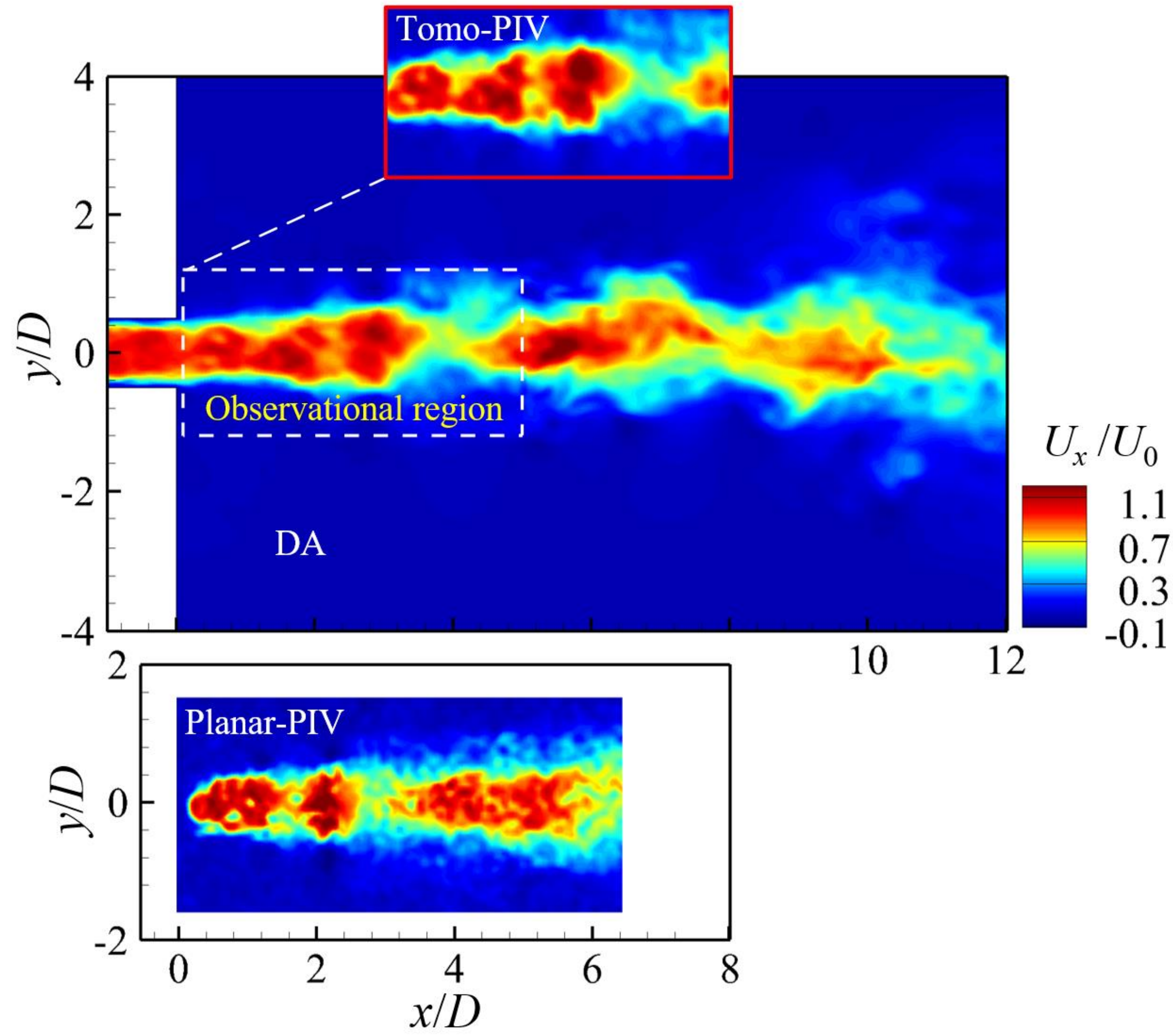

Fig. 7 Instantaneous streamwise velocity fields obtained by tomo-PIV, planar-PIV and DA. The tomo-PIV and planar-PIV results are only for qualitative comparison as they were measured separately.

Fig. 8 shows a quantitative comparison of the streamwise velocity distributions and their velocity fluctuations at the downstream location $x/D = 2$ and 4 . This comparison is a statistical validation of the DA scheme on the reproduction of the flow field. To obtain converged and smoothed data, the velocity was time- and azimuthal-averaged (azimuthal locations for every 2 degrees for the three-dimensional data but only for every 180 degrees for the planar-PIV measurements). The planar-PIV measurements served as the reference When compared to the tomo-PIV results, the planar-PIV measurements showed a slight discrepancy due to measurement uncertainty. The tomo-PIV over-estimated the mean velocity in the jet column at $x/D = 4$ by 4%

and in the initial jet shear layer at $x/D = 2$ by much larger percentage. It also determined the velocity fluctuation intensity, which was 17% higher than that of the planar-PIV measurement in the jet column at $x/D = 4$.

Fig. 5 covers the measurement uncertainty of the tomo-PIV, and we now focus on the DA results. DA accurately predicted the mean velocity at both $x/D = 2$ and 4, but the under-estimation of the velocity fluctuation was observed at $x/D = 2$ by 25%. This discrepancy resulted from the inflow boundary condition on which the imposed flow fluctuation was lower than that in the experiment. Note that the measured flow was not strictly representative of the fully developed pipe jet. DA recovered the flow fluctuation by the constraints of the observations. This constraint effectiveness was improved with the jet development toward the downstream direction, which resulted in agreement of the velocity fluctuation and planar-PIV data at $x/D = 4$.

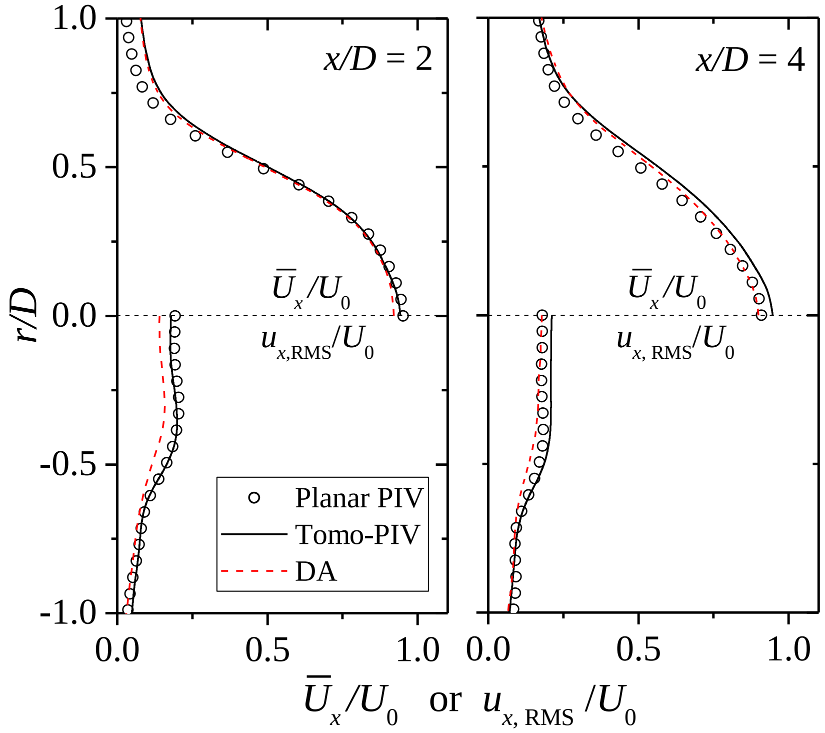

Fig. 8 Mean and fluctuating streamwise velocity distributions obtained by tomo-PIV, planar-PIV and DA.

Once the flow had accurately recovered, the accompanying pressure field was obtained. This was computed by solving the Poisson equation (Eq. (17)) in the DA solver. However, instead of solving the Poisson equation directly from the PIV results, the DA-based pressure determination method solves the Poisson equation based on the assimilated flow fields. These flow fields approach the tomo-PIV data within the tolerance of the measurement uncertainty but are subject to less effects of measurement errors and boundary conditions. Fig. 9 (Multimedia view) shows the instantaneous pressure (natural pressure) isosurface determined by DA using the direct mode. The accuracy of this pressure determination method has been already validated using the large-eddy simulation (LES) data[21], and the present pressure field was also believable. As expected, vortex-ring-like structures were captured by DA in the pressure field, with the dark rings denoting negative pressure and the light rings representing positive pressure. This pressure pattern was confirmed by the streamwise velocity fields on the centre planes, i.e., the negative pressure isosurfaces were located surrounding the fluid puffs where the vortex rings exist while the positive pressure isosurfaces were located between two successive fluid puffs away from the vortex rings.

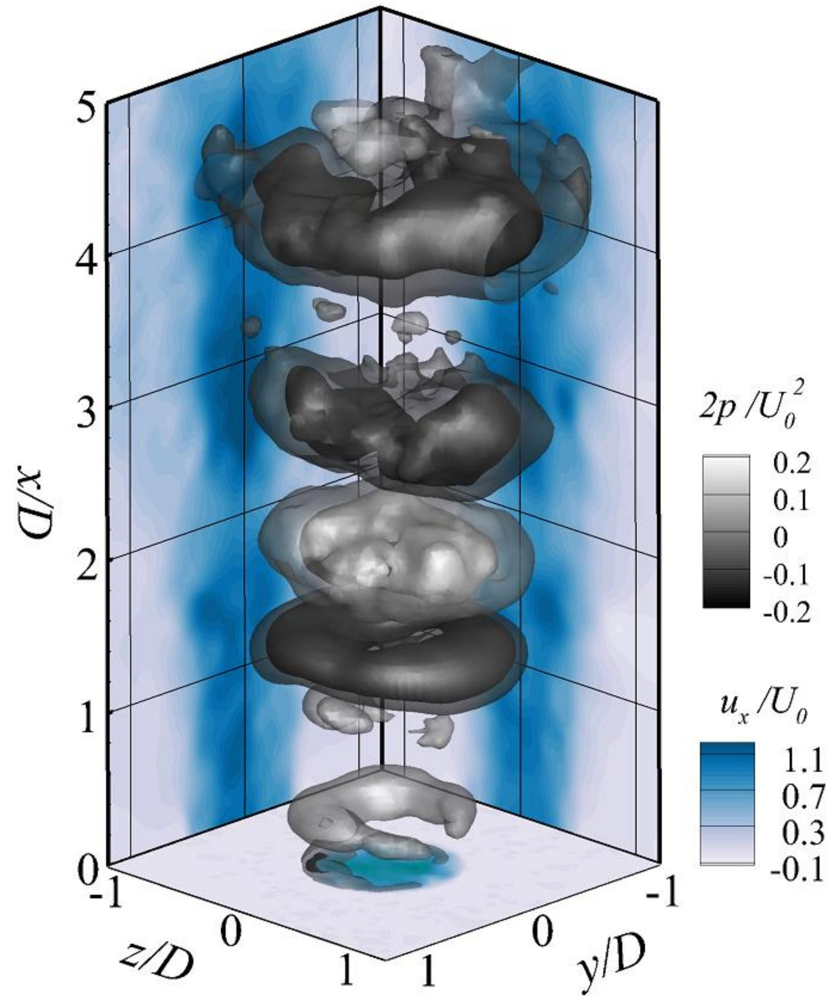

Fig. 9 Instantaneous pressure isosurfaces ($2p/U_0^2 = \pm 0.05$ & $\pm$ 0.1) recovered by DA. Flow snapshots on the streamwise centre planes and the nozzle exit plane are also shown. (Multimedia view)

4.2 Details of the flow and pressure assimilation

Following the overview of the DA results, more details of the flow and pressure fields are discussed. As noted in Fig. 1, a typical feature of the sequential DA is the piecewise smooth of the temporal variations. The DA time step and the time interval between the observations were $\Delta t = 0.002$ and $\Delta T = 0.01$, respectively, which yielded the implantation of the observations into the DA computation every 5 time steps. The temporal variation in velocity and pressure at the location

$y/D = 0.5$ and $x/D = 2$ is shown in Fig. 10. Each quantity predicted by DA experienced an abrupt switching every 5 time steps when the observations were present (see the full time DA data). This switching is indeed unnatural while the smooth temporal variation is expected in a naturally developed flow. The small-time variation in each quantity within the observational time interval did not strictly follow the trend of the observations, specifically for the y-component velocity (in depth direction shown in Fig. 10b). The trend consistency of the small-time variation depended on the relative contribution of the observation constraint, i.e., when the pure simulation is prone to producing a flow approaching the observations, the forcing $\boldsymbol{F}$ should be significantly small. Thus, the switching at the observational instance will be quite small and will yield a smooth variation in time. For the present flow configuration, the flow development was strongly dependent on the inflow condition and the computational mesh resolution. The observation constraint played a major role in forcing how the flow varied along with the observations. The abrupt switching of the flow quantities from the unforced instance to the observation-constraint instance is a common feature in sequential DA schemes[23, 49]. However, only the flow quantities at the observational instances were considered as giving rise to the smooth variation in the velocities and pressure over time (see the red DA data). Fig. 10 also shows the temporal variations in the tomo-PIV data. The DA results have a similar trend but much lower random fluctuations. This result suggests that the flow enhancement function of the DA scheme played a major part in smoothing the flow temporal variation which was most likely subject to random errors in tomo-PIV measurements.

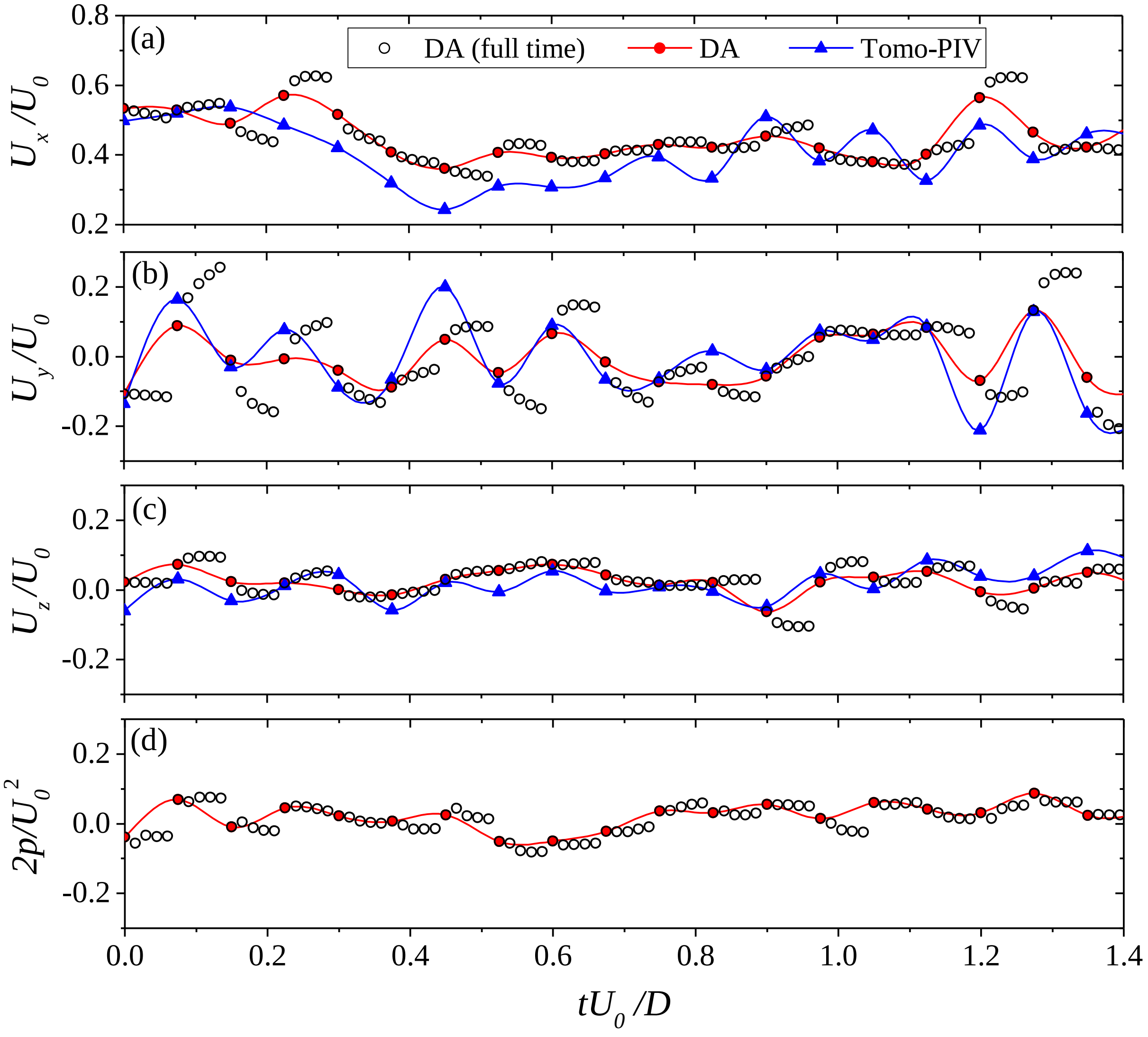

Fig. 10 Temporal variations in the velocity components (a-c) and pressure (d) at $y/D = 0.5$ and $x/D = 2$. DA (full time): DA data at very time step; DA: DA data at only the observational instances; Tomo-PIV: Original tomo-PIV data.

A global view of the flow variation is shown in Fig. 11 (Multimedia view). The tomo-PIV measurement (left column) and the corresponding DA prediction (right column) were extracted at the same time. The temporal variation at three successive observational instances with an interval $\Delta T = 0.01$ is shown from top to down. Tomo-PIV could not acquire the flow data from inside the nozzle and even missed some of the flow close to the nozzle exit. The downstream convection of the large-scale flow structures is shown in Fig. 11(a, c, e), but the small structures were exhibited in a random way and contaminated the flow field. The DA scheme was implemented with tolerance of measurement uncertainty and thus treated the random small scales as measurement noise, as shown in Fig. 11(b, d, f). The flow fluctuation in the upstream region $x/D < 2$ in DA was not as well excited as that in tomo-PIV measurement, probably because of the differences in the inflow condition as previously mentioned. In fact, this inflow condition is quite difficult to consider precisely in conventional numerical simulations even using the inflow boundary condition generator[50, 51]. While the DA scheme also provides a boundary condition approach[52], this study did not focus on the inflow condition itself, but rather on an alternative way to recover the flow from a synthetic unreal inflow. Flow recovery was augmented in further downstream regions as that at $x/D > 4$.

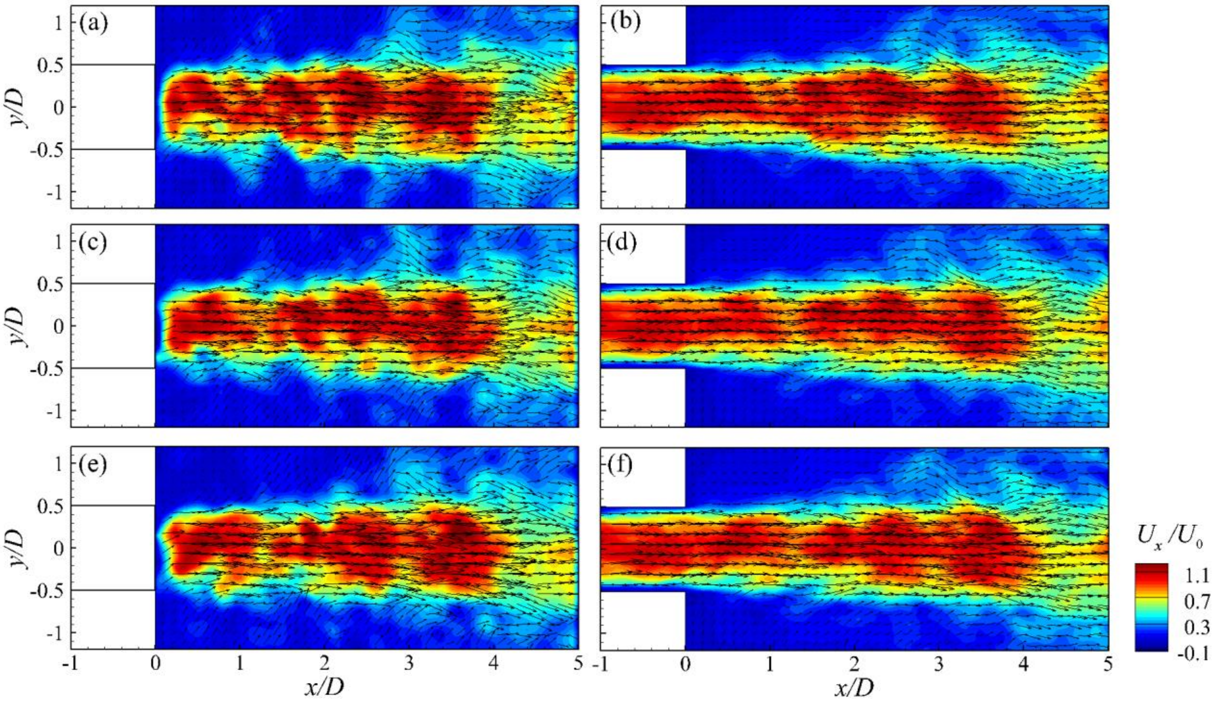

Fig. 11 Spatial distribution of the streamwise velocity with time interval $\Delta T = 0.01$ s: (a, c, e) tomo-PIV; (b, d, f) DA. (Multimedia view)

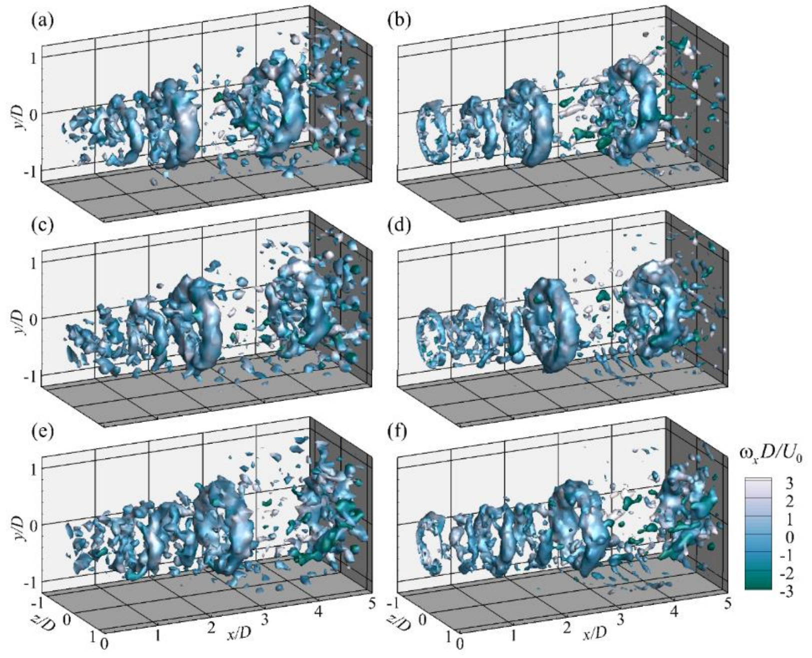
(a)
(b)
(c)
(d)
(e)
(f)
y/D
1
0
-1
z/D
x/D
0
1
2
3
4
5
ω_x D/U_0
3
2
1
0
-1
-2
-3

Fig. 12 Isosurface of $QD/U_0 = 10$ coloured by the streamwise vorticity with time interval $10\Delta T = 0.1$ s: (a, c, e) tomo-PIV; (b, d, f) DA. (Multimedia view)

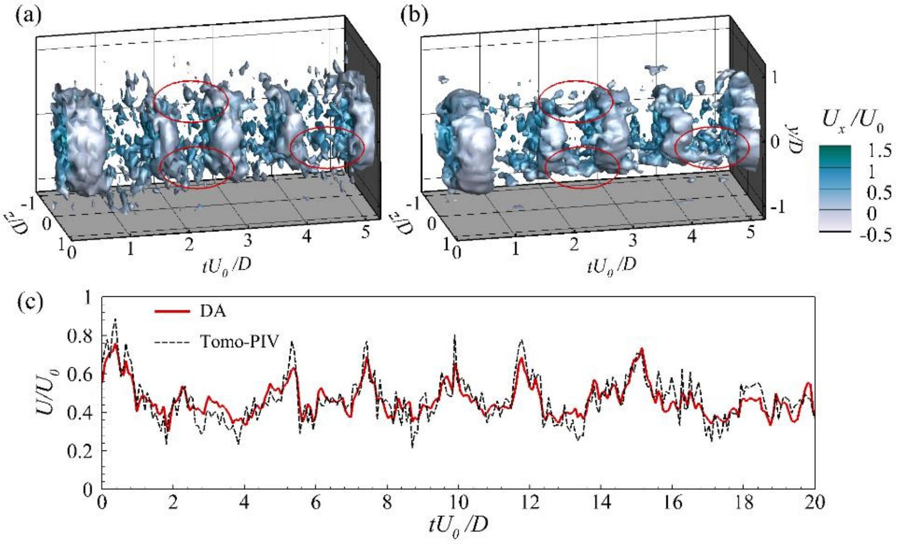

Fig. 13 Spatiotemporal plot of the vortical structures (isosurface of $QD/U_0 = 10$ coloured by the streamwise velocity) at $x/D = 2$: (a) tomo-PIV; (b) DA. The velocity sequences at $x/D = 2$ and $y/D = 0.5$ are also compared in (c).

Vortex rings were observed due to the nature of this low-Reynolds-number jet flow. In Fig. 12 (Multimedia view), the DA data were extracted from the observational region (Fig. 12 right column) and compared to the tomo-PIV measurements (Fig. 12 left column). The time interval was set to $10\Delta T$ to visualise the downstream convection of the vortex rings more clearly. The vortical structures in the tomo-PIV data were less organised due to measurement error, especially at $x/D < 2$. Additionally, more vortical fragments were observed in the shear layer, especially after the vortex breakdown. In contrast, the DA results contained rather clear vortex ring structures convecting downstream by filtering a large portion of the vortical fragments. In fact, on closer inspection of the temporal sequence, the majority of the vortical fragments in the tomo-PIV results were not time correlated (Fig. 13a). The red circles in Fig. 13 mark the temporal variation at small scales, which have a narrow extension in the time direction indicating random noise. DA smoothed the large-scale vortical ring by eliminating the measurement noise and induced temporal correlation for small scales as illustrated by the elongated vortices (marked in red circles) in Fig. 13b. The quantitative comparison is shown in Fig. 13c, and reasonable agreement between the DA results and the measurement data can be seen. A clear discrepancy in the velocity sequence is the reduction of the DA velocity value in instances where the tomo-PIV data experienced abrupt peaks, which is indicative of the error elimination mechanism of DA and also a slight under-estimation of the velocity fluctuation (Fig. 8).

Fig. 14 presents the probability density functions (PDFs) of the streamwise fluctuating velocities obtained by different schemes for deeper analysis. The planar-PIV data was used as the reference for validation. The tomo-PIV measurement had a significantly higher probability of negative fluctuating velocity, i.e., $-1.5 < u_x'/u_{x,\mathrm{RMS}} < -0.5$, but a slightly lower probability of positive fluctuating velocity $0 < u_x'/u_{x,\mathrm{RMS}} < 1$ at both downstream locations. The over-estimation of the probability around $u_x'/u_{x,\mathrm{RMS}} = 2$ by tomo-PIV was also observed. This dynamic feature is well visualised in Fig. 13c. The abrupt peaks of the tomo-PIV velocity at approximately $tU_0/D = 4.6$, 6.6, 10 and 12 contributed to the over-estimation of the PDF around $u_x'/u_{x,\mathrm{RMS}} = 2$. The frequent small-scale fluctuations at $tU_0/D = 2$, 4, 6, 8.4, etc. played an important role in increasing the PDF for -1.5 < $u'_x/u_{x,\mathrm{RMS}}$ < -0.5. With the attenuation of the abrupt peaks in the DA results, a decrease in the PDF at $u'_x/u_{x,\mathrm{RMS}} = 2$ was achieved, being closer to the planar-PIV data in the figure. The PDFs predicted by DA agreed with the planar-PIV measurement, demonstrating that DA improved the flow's dynamic features statistically.

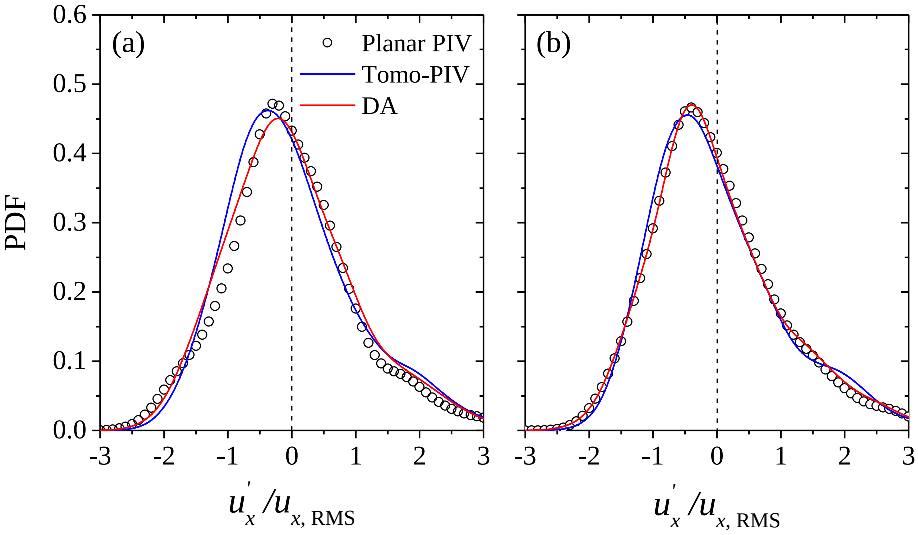

Fig. 14 Comparison of the PDFs of the streamwise fluctuating velocities at $y/D = 0.5$: (a) $x/D = 2$; (b) $x/D = 4$.

Divergence error, one of the main errors in tomo-PIV measurements, has serious effects on pressure determination. Because PIV algorithm is based on the image processing using cross-correlation of the gray-scale distribution to compute velocity vectors, it lacks the strict constraint of flow mass conservation in a controlled volume. The divergence error is expressed as $\varepsilon_{\mathrm{div}} = \nabla \cdot \boldsymbol{U}$; when substituting this expression into Eq. (15), the following form of the pressure equation is obtained,

$$\nabla \cdot \left(\frac{1}{a_P} \nabla p\right) = \sum_f S \cdot \left[\frac{\boldsymbol{H}(\boldsymbol{U})}{a_P} - \varepsilon_{\mathrm{div}}\right]_f . \tag{19}$$

Eq. (18) suggests that the Laplacian of the pressure is linearly dependent on the divergence error, and thus the absolute pressure distribution is much more sensitive. Here, we calculate the joint PDFs between ddx and $ddyz$, which are defined as

$$ddx = \frac{D}{U_0}\left(\frac{\partial U_x}{\partial x}\right) \tag{20}$$

$$ddyz = -\frac{D}{U_0}\left(\frac{\partial U_y}{\partial y} + \frac{\partial U_z}{\partial z}\right) \tag{21}$$

The inclined dashed lines in Fig. 15 represent the divergence free properties of the joint PDFs. The tomo-PIV results significantly deviated from the divergence free line at both downstream locations, as shown in Fig. 15(a, c). The DA results were improved, as presented in Fig. 15(b, d). Indeed, the divergence free constraint was naturally implemented in the DA procedure by solving the primary equations. Thus, the assimilated flow did not approach the observations with a well-converged computational residual.

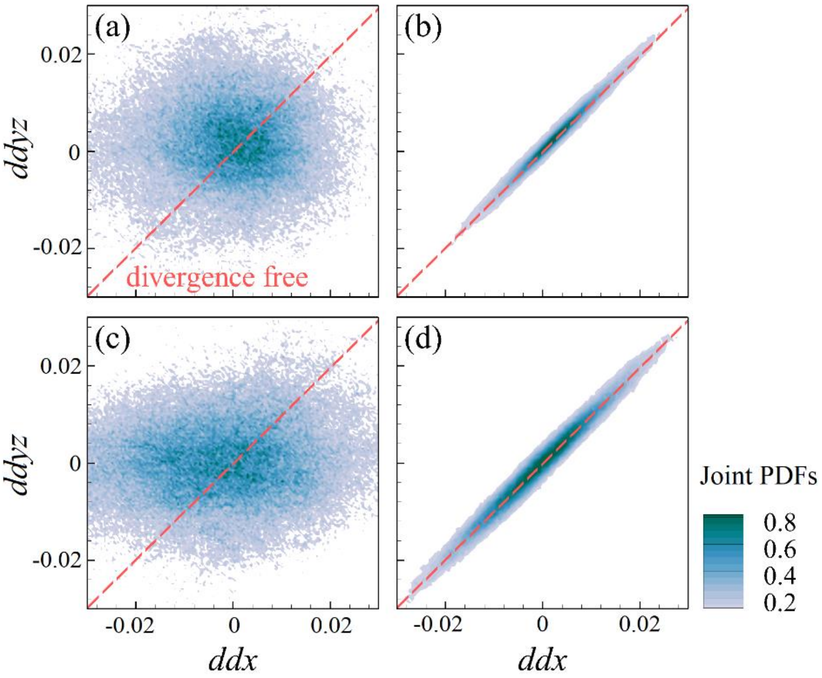

Fig. 15 Joint PDFs between *ddx* and *ddyz* at: (a, b) $x/D = 2$; (c, d) $x/D = 4$. The left column shows the tomo-PIV data, and the right shows presents the DA data.

As shown in Fig. 10, the sequential DA reproduced piecewise-smooth flow quantities, while only the data at the observational instances ($\Delta T = 0.01$ s) were selected as the DA outputs. Fig. 16 presents the power spectral densities (PSDs) of the streamwise velocity at the radial location $r/D = 0.5$ at two downstream stations. The PSD of the planar-PIV data was computed using 3,000 snapshots and data velocity data at $y/D = \pm 0.5$. The tomo-PIV and DA results used 500 snapshots at 180 uniformly distributed azimuthal locations to determine the well converged curves. At $x/D = 2$, the main Strouhal number (St) peaked at $St = 0.23$, 0.45 and 0.67. These values were well captured by both the planar-PIV and tomo-PIV measurements, and also by the DA prediction. At $x/D = 4$, the main peaks moved to $St = 0.28$, 0.42 and 0.60 and were affected by the nonlinear convection process. They were also roughly captured by all of the schemes. The differences in the peak order captured by the different methods may be a result of the data size used in the PSD computations. High spectra plateaus were observed in the tomo-PIV data due to either the measurement noise in the flow temporal sequence or the low mesh resolution. It is noted that the interpolation of the tomo-PIV results to the fine DA mesh induces error. This noise level was much lower in the planar-PIV data, as indicated by the PSD curves decaying on a -5/3 slope. The PSDs of the DA data agreed well with those of the tomo-PIV measurements at $St < 1$, but significant deviations were observed at higher St numbers. Such deviations suggest that the large-scale motion of the flow in the tomo-PIV data was completely reproduced by DA, while the error elimination worked in the range of small-scale structures. The DA spectra had a decaying slope that was slightly steeper than the -5/3 law, indicating the absence of small-scale turbulence in the assimilated flows. Nevertheless, this steeper slope at a high St number is common in conventional numerical simulations and in this study was most likely induced by the combined effects of the artificial viscosity of the coarse mesh and the damping of small fluctuations due to the forcing.

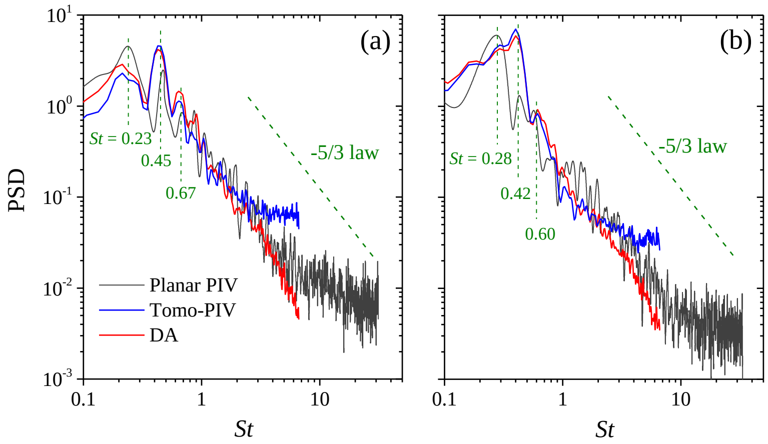

Fig. 16 PSDs of the streamwise velocity at $r/D = 0.5$ and: (a) $x/D = 2$; (b) $x/D = 4$.

Based on the well-recovered flow field, the pressure was determined by either the direct mode (natural pressure) implemented together with the DA solver with the time step $\Delta t = 0.002$ s, or by the separate mode of solving the Poisson equation after the DA computation with the time interval $\Delta T = 0.01$ s. Fig. 17 shows the temporal sequences of the pressure fields determined by these two methods. Both methods obtained the pressure distributions reasonably well by capturing the signatures of the vortex rings and their downstream convection. Even with the abrupt switching in the flow fields as shown in Fig. 10, the pressures calculated using the direct mode in Fig. 17(a, c, d) did not show any peculiar distributions due to the relatively low contribution of the time derivative term on the pressure determination. In contrast, the pressure fields calculated using the separate mode, as shown in Fig. 17(b, d, f), were contaminated by high levels of numerical noise due to the absence of $\boldsymbol{F}$ term and thus the lack the repeated momentum-pressure corrections. A more detailed comparison of these two approaches for pressure determination is shown in Fig. 18. The spatiotemporal plots of the pressure fields in Fig. 18(a-b) show the accuracy of both modes at capturing the spatiotemporal evolution of the pressure, with the inclined stripes indicating the downstream convection of the vortex rings. While Fig. 18(c-d) shows agreement among the temporal evolution of the pressure signals, the direct mode of the pressure determination is recommended due to the convenience in the calculation procedure and the signal-to-noise ratio in space and time.

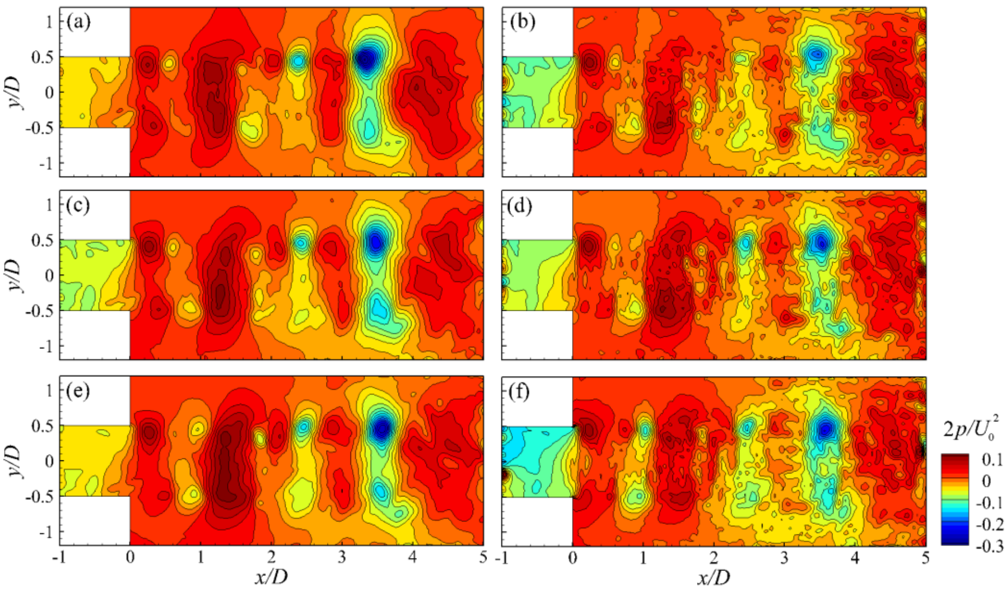

Fig. 17 Instantaneous pressure fields determined by DA using the direct mode (left) and separate mode (right). The time interval for both pressure sequences is $\Delta T = 0.01$ s.

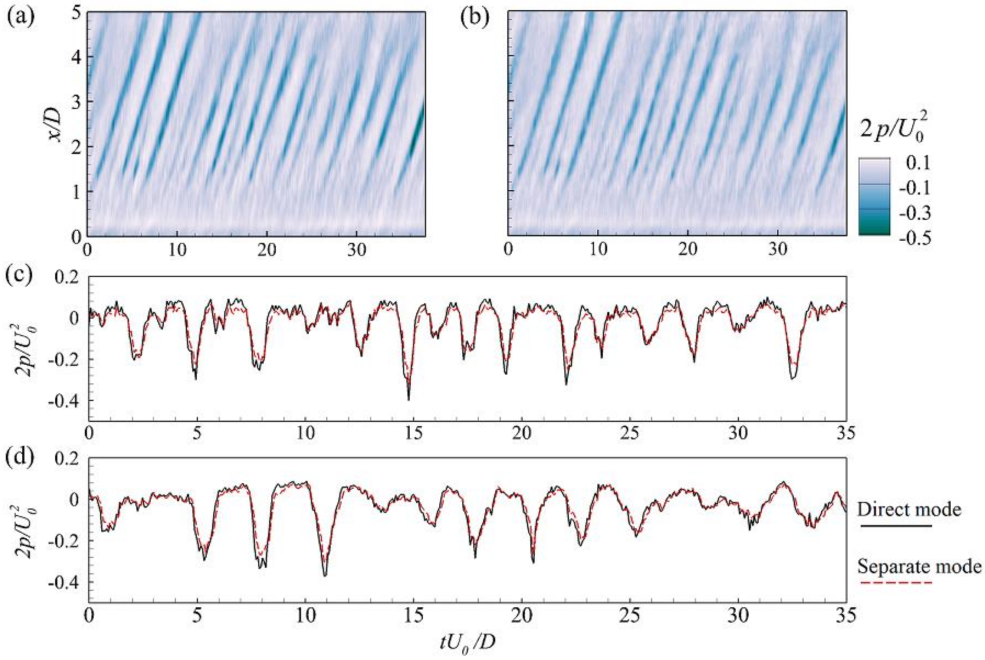

Fig. 18 Spatiotemporal plot of the pressure at $y/D = 0.5$ and $0 < x/D < 5$ determined DA using: (a) the direct mode; (b) the separate mode. The time sequences of the pressure at $y/D = 0.5$, (c) $x/D = 2$, (d) $x/D = 4$ are also shown.

5. Conclusions

The present study concentrated on the enhancement of the flow fields by reducing measurement error and by determining the spatiotemporal distribution of pressure data. The tomo-PIV system, with two high-speed cameras and a screen-split configuration, was used to acquire three-dimensional velocity fields, which were subsequently used as the observations in the DA. The adjoint-based sequential DA scheme was used to recover the flow fields with high-fidelity and less measurement error. Pressure was determined by either directly implementing the DA solver or by solving the Poisson equation on the DA-recovered flow fields.

The adjoint-based sequential DA was improved under the frame work of our previous study by implementing a threshold function to cope with the measurement uncertainty explicitly. Although the tomo-PIV measurement was performed on a thick domain with considerable large error, the results demonstrated that the sequential DA recovered the jet's mean flow and that the fluctuation which agreed reasonably well with the benchmark planar-PIV measurements. Due to the sequential nature of the observation implantation, the flow fields experienced a piecewise-smooth temporal variation and thus only the temporal sequence of the fields at the observational instances was selected as the DA output. The flow errors were significantly reduced and the divergence condition of the flow fields was substantially improved by the DA. It also improved the statistics of the flow dynamical features by improving the PSD and PDF.

The three-dimensional pressure fields were reasonably recovered by capturing the spatial patterns and downstream convection of the vortex rings. Both the direct and separate modes determined the pressure fields well. However, higher signal-to-noise ratio was achieved by the direct mode; the absence of $\boldsymbol{F}$ term and thus the lack the repeated momentum-pressure corrections was responsible for the relatively low signal-to-noise ratio in the separate-mode computation. Applications are recommended for three dimensional flow dynamic researches and acoustic source detection in aeronautical engineering using the present DA scheme.

Acknowledgements

The authors gratefully acknowledge financial support for this study from the National Natural Science Foundation of China (11725209, 12002208), the Natural Science Foundation of Shanghai (20ZR1425700), and the Engineering and Physical Sciences Research Council of the UK (EP/P004377/1).

Data Availability

The data that support the findings of this study are available from the corresponding author upon reasonable request.

Conflict of Interest

The authors have no conflicts to disclose.

References

1. D. Fan, D. D. Borup, C. J. Elkins, and J. K. Eaton, "Measurements in discrete hole film cooling behavior with periodic freestream unsteadiness," Experiments in Fluids **59**, 37 (2018).
2. L. Gan, T. B. Nickels, and J. R. Dawson, "An experimental study of a turbulent vortex ring: a three-dimensional representation," Experiments in Fluids **51**, 1493 (2011).
3. G. E. Elsinga, F. Scarano, B. Wieneke, and B. Oudheusden, "Tomographic particle image velocimetry," Experiments in Fluids **41**, 933 (2006).
4. D. Loshin, *Data Enhancement: In Practitioners Guide to Data Quality Improvement* (Morgan Kaufmann OMG Press, Amsterdam, Boston, Heidelberg, London, New York, Oxford, Paris, San Diego, San Francisco, Singapore, Sydney, Tokyo 2011).
5. K. U. Kempaiah, F. Scarano, G. E. Elsinga, B. W. v. Oudheusden, and L. Bermel, "3-dimensional particle image velocimetry based evaluation of turbulent skin-friction reductionby spanwise wall oscillation," Physics of Fluids **32**, 085111 (2020).
6. B. Wieneke, "Volume self-calibration for 3D particle image velocimetry," Experiments in Fluids **45**, 549 (2008).
7. H. G. Maas, A. Gruen, and D. Papantoniou, "Particle tracking velocimetry in three-dimensional flows," Experiments in Fluids **15**, 133 (1993).
8. G. E. Elsinga, B. Wieneke, F. Scarano, and A. Schröder, *Tomographic 3D-PIV and Applications. In: Particle Image Velocimetry. Topics in Applied Physics.* (Springer, Berlin, Heidelberg, 2007).
9. N. Matteo, K. J. Batenburg, and F. Scarano, "Motion tracking-enhanced MART for tomographic PIV," Measurement Science and Technology **21**, 035401 (2010).
10. D. Schanz, S. Gesemann, and A. Schrder, "Shake-The-Box: Lagrangian particle tracking at high particle image densities," Experiments in Fluids **57**, 70 (2016).
11. C. Y. Wang, Q. Gao, H. P. Wang, R. J. Wei, and J. J. Wang, "Divergence-free smoothing for volumetric PIV data," Experiments in Fluids **57**, 1 (2016).
12. B. W. V. Oudheusden, "PIV-based pressure measurement," Measurement Science and Technology **24**, 032001 (2013).
13. X. Liu, and J. R. Moreto, "Pressure reconstruction of a planar turbulent flow field within a multiply connected domain with arbitrary boundary shapes," Physics of Fluids **33**, 101703 (2021).
14. J. Van der Kindere, A. Laskari, B. Ganapathisubramani, and R. De Kat, "Pressure from 2D snapshot PIV," Experiments in Fluids **60**, 32 (2019).
15. R. de Kat, and B. W. V. Oudheusden, "Instantaneous planar pressure determination from PIV in turbulent flow," Experiments in Fluids **52**, 1089 (2011).
16. R. de Kat, B. W. V. Oudheusden, and F. Scarano, *Instantaneous planar pressure field determination around a square-section cylinder based on time resolved stereo-PIV.* (Lisbon, Portugal, 2008).
17. T. Tronchin, L. David, and A. Farcy, "Loads and pressure evaluation of the flow around a flapping wing from instantaneous 3D velocity measurements," Experiments in Fluids **56**, 1 (2015).
18. J. F. G. Schneiders, S. Pröbsting, R. P. Dwight, B. W. v. Oudheusden, and F. Scarano, "Pressure estimation from single-snapshot tomographic PIV in a turbulent boundary layer," Experiments in Fluids **57**, 53 (2016).
19. M. Novara, and F. Scarano, *Lagrangian acceleration evaluation for tomographic PIV: a particle-tracking based approach* (Lisbon, Portugal, 2012).

20. Z. Pan, J. Whitehead, S. Thomson, and T. Truscott, "Error propagation dynamics of PIV-based pressure field calculations: how well does the pressure Poisson solver perform inherently?," Measurement Science and Technology **27**, 084012 (2016).

21. C. He, Y. Liu, and L. Gan, "Instantaneous pressure determination from unsteady velocity fields using adjoint-based sequential data assimilation," Physics of Fluids **32**, (2020).

22. G. Evensen, *Data assimilation. The ensemble Kalman filter* (Springer, Germany, 2009).

23. M. Meldi, and A. Poux, "A reduced order model based on Kalman filtering for sequential data assimilation of turbulent flows," Journal of Computational Physics **347**, 207 (2017).

24. H. Kato, A. Yoshizawa, G. Ueno, and S. Obayashi, "A data assimilation methodology for reconstructing turbulent flows around aircraft," Journal of Computational Physics **283**, 559 (2015).

25. S. Pawar, S. E. Ahmed, O. San, A. Rasheed, and I. M. Navon, "Long short-term memory embedded nudging schemes for nonlinear data assimilation of geophysical flows," Physics of Fluids **32**, 076606 (2020).

26. Z. Deng, C. He, X. Wen, and Y. Liu, "Recovering turbulent flow field from local quantity measurement: turbulence modeling using ensemble-Kalman-filter-based data assimilation," Journal of Visualization 1 (2018).

27. H. Xiao, J. L. Wu, J. X. Wang, R. Sun, and C. J. Roy, "Quantifying and reducing model-form uncertainties in Reynolds-averaged Navier–Stokes simulations: A data-driven, physics-informed Bayesian approach," Journal of Computational Physics **324**, 115 (2015).

28. S. Pawar, S. E. Ahmed, O. San, and A. Rasheed, "Data-driven recovery of hidden physics in reduced order modeling of fluid flows," Physics of Fluids **32**, 036602 (2020).

29. C. He, Y. Liu, and L. Gan, "A data assimilation model for turbulent flows using continuous adjoint formulation," Physics of Fluids **30**, 105108 (2018).

30. C. He, Y. Liu, L. Gan, and L. Lesshafft, "Data assimilation and resolvent analysis of turbulent flow behind a wall-proximity rib," Physics of Fluids **31**, 025118 (2019).

31. A. P. Singh, and K. Duraisamy, "Using field inversion to quantify functional errors in turbulence closures," Physics of Fluids **28**, 407 (2016).

32. E. J. Parish, and K. Duraisamy, "A paradigm for data-driven predictive modeling using field inversion and machine learning," Journal of Computational Physics **305**, 758 (2016).

33. Y. J. Jeon, G. Gomit, T. Earl, L. Chatellier, and L. David, "Sequential least-square reconstruction of instantaneous pressure field around a body from TR-PIV," Experiments in Fluids **59**, 27 (2018).

34. K. Agarwal, O. Ram, J. Wang, Y. Lu, and J. Katz, "Reconstructing velocity and pressure from noisy sparse particle tracks using constrained cost minimization," Experiments in Fluids **62**, 75 (2021).

35. M. Lemke, and J. Sesterhenn, "Adjoint-based pressure determination from PIV data in compressible flows—validation and assessment based on synthetic data," European Journal of Mechanics-B/Fluids **58**, 29 (2016).

36. M. Lemke, "Adjoint based data assimilation in compressible flows with application to pressure determination from PIV data," Technische Universität Berlin, 2015.

37. V. Mons, J.-C. Chassaing, and P. Sagaut, "Optimal sensor placement for variational data assimilation of unsteady flows past a rotationally oscillating cylinder," Journal of Fluid Mechanics **823**, 230 (2017).

38. C. He, and Y. Liu, "Time-resolved reconstruction of turbulent flows using linear stochastic estimation and sequential data assimilation," Physics of Fluids **32**, 75106 (2020).

39. C. Othmer, "A continuous adjoint formulation for the computation of topological and surface sensitivities of ducted flows," International Journal for Numerical Methods in Fluids **58**, 861 (2008).

40. L. Armijo, "Minimization of functions having Lipschitz continuous first partial derivatives," Pacific Journal of

Mathematics **16**, 1 (1966).

41. H. Jasak, "Error analysis and estimation for the finite volume method with applications to fluid flows," Imperial College London, 1996.

42. C. He, Y. Liu, and L. Gan, "Dynamics of the jet flow issued from a lobed nozzle: tomographic particle image velocimetry measurements," International Journal of Heat and Fluid Flow **89**, 108795 (2021).

43. P. M. Bardet, P. F. Peterson, and Ö. Savaş, "Split-screen single-camera stereoscopic PIV application to a turbulent confined swirling layer with free surface," Experiments in Fluids **49**, 513 (2010).

44. N. Worth, and T. Nickels, "Time-resolved volumetric measurement of fine-scale coherent structures in turbulence," Physical Review E **84**, 025301 (2011).

45. L. Gan, J. I. Cardesa-Duenas, D. Michaelis, and J. R. Dawson, *Comparison of tomographic PIV algorithms on resolving coherent structures in locally isotropic turbulence.* (Lisbon, Portugal, 2012).

46. C. He, Y. Liu, and S. Yavuzkurt, "Large-eddy simulation of circular jet mixing: Lip- and inner-ribbed nozzles," Computers & Fluids **168**, 245 (2018).

47. A. Sciacchitano, B. Wieneke, and F. Scarano, "PIV uncertainty quantification by image matching," Measurement Science & Technology **24**, 045302 (2013).

48. B. M. Wilson, and B. L. Smith, "Uncertainty on PIV mean and fluctuating velocity due to bias and random errors," Measurement Science & Technology **24**, 035302 (2013).

49. L. Yang, A. Narayan, and P. Wang, "Sequential data assimilation with multiple nonlinear models and applications to subsurface flow," Journal of Computational Physics **346**, 356 (2017).

50. L. Davidson, "Using isotropic synthetic fluctuations as inlet boundary conditions for unsteady simulations," Advances and Applications in Fluid Mechanics **1**, 1 (2007).

51. G. R. Tabor, and M. H. Baba-Ahmadi, "Inlet conditions for large eddy simulation: A review," Computers & Fluids **39**, 553 (2010).

52. A. Gronskis, D. Heitz, and E. Mémin, "Inflow and initial conditions for direct numerical simulation based on adjoint data assimilation," Journal of Computational Physics **242**, 480 (2013).

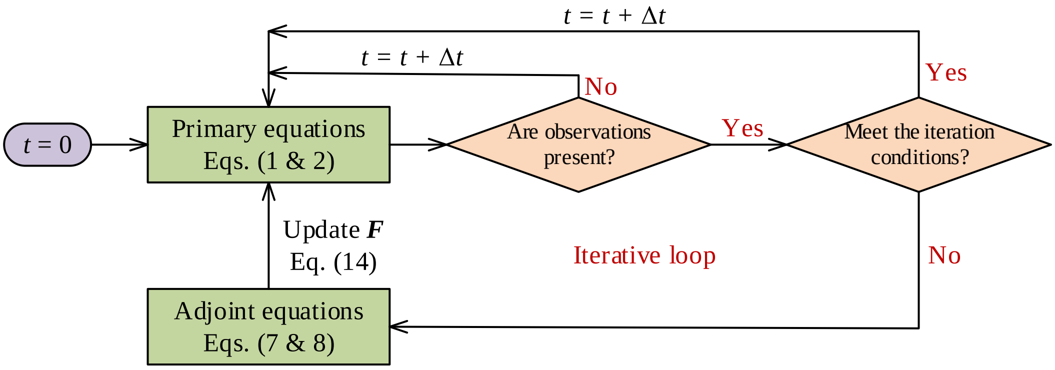
t = t + Δt
t = t + Δt
No
Yes
t = 0
Primary equations
Eqs. (1 & 2)
Are observations present?
Yes
Meet the iteration conditions?
Update F
Eq. (14)
Iterative loop
No
Adjoint equations
Eqs. (7 & 8)

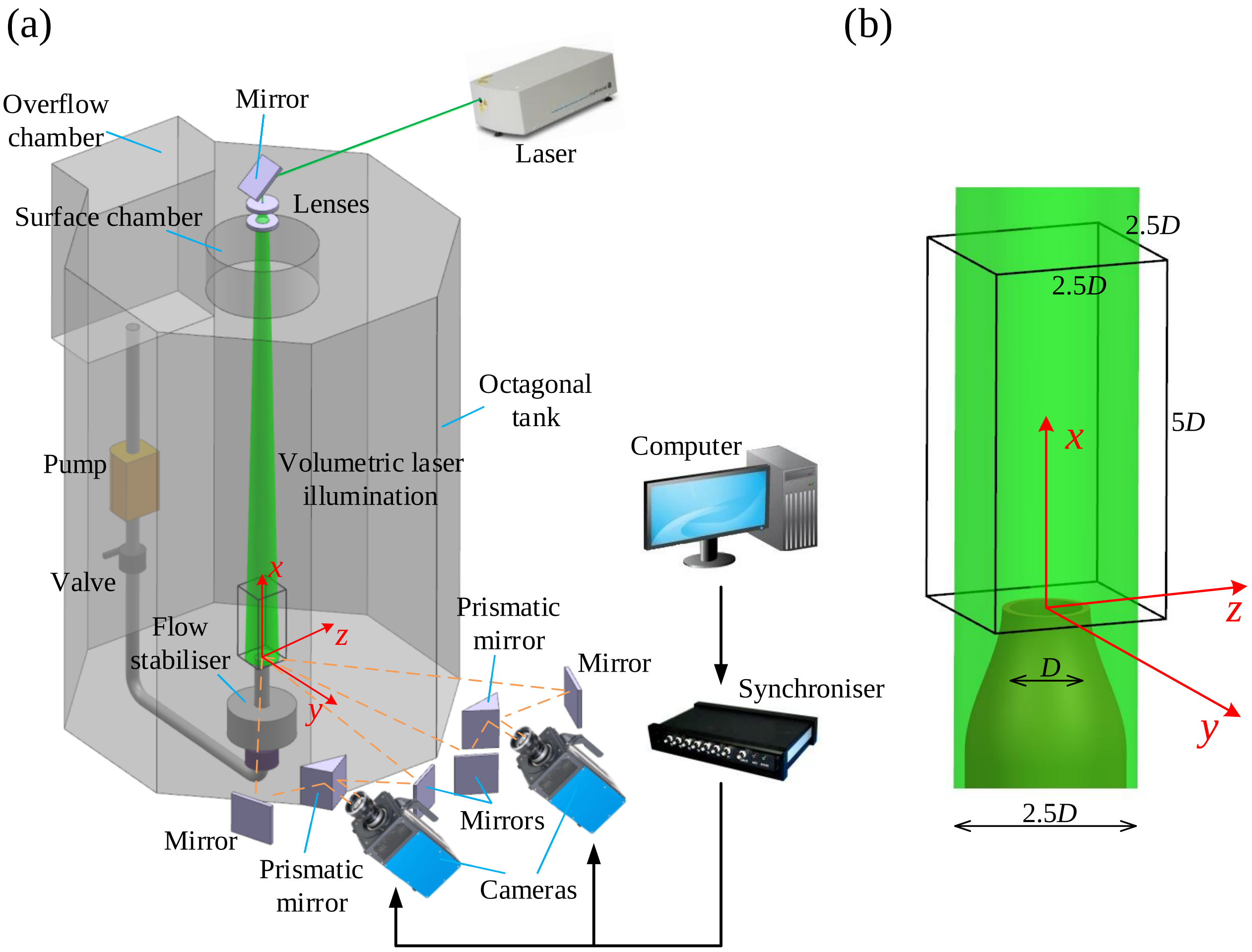
(a)
(b)
Overflow chamber
Mirror
Laser
Lenses
Surface chamber
Octagonal tank
Pump
Volumetric laser illumination
Computer
Valve
x
z
y
Flow stabiliser
Prismatic mirror
Mirror
Synchroniser
Mirror
Mirrors
Prismatic mirror
Cameras
2.5D
2.5D
5D
x
z
y
D
2.5D

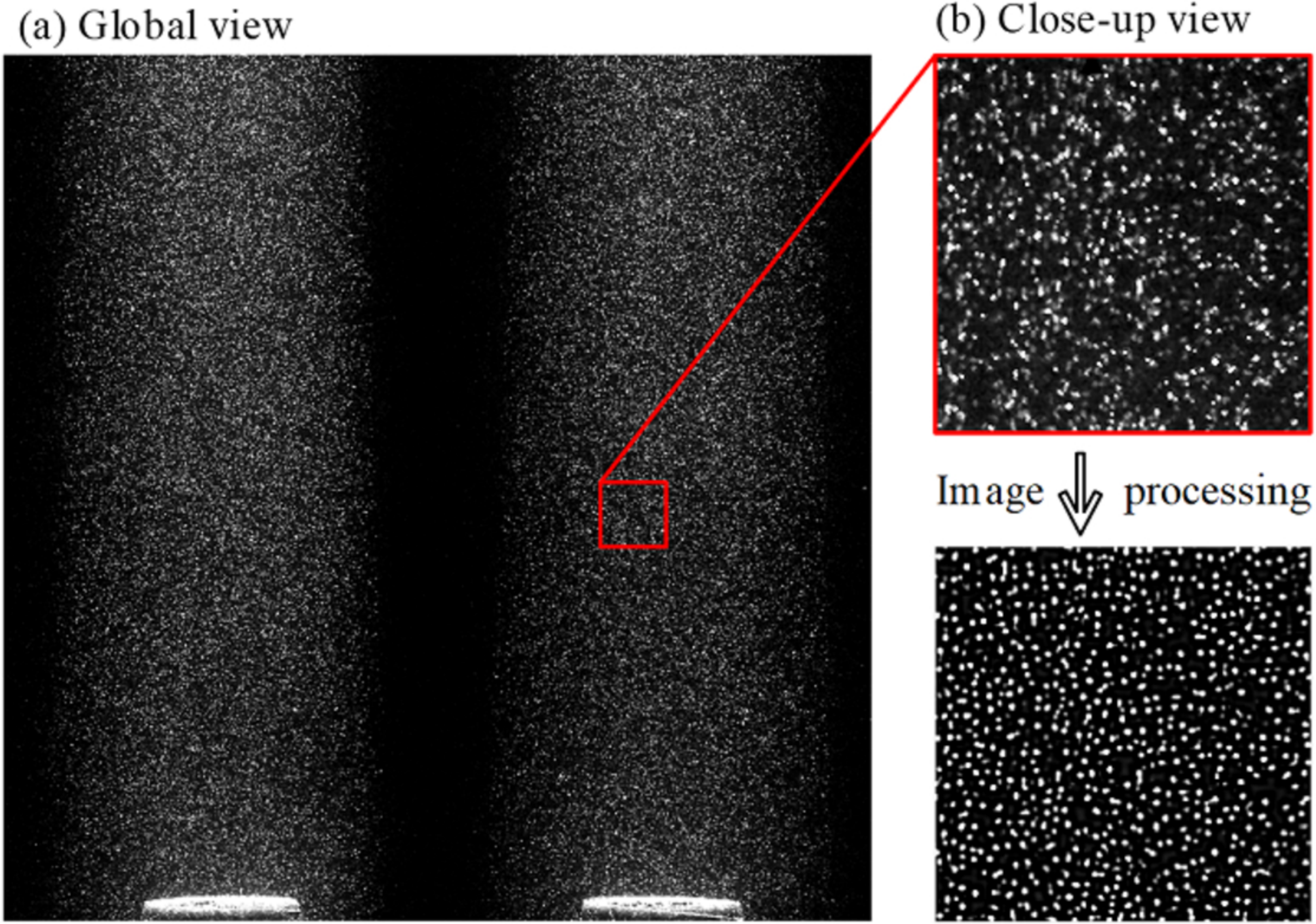
(a) Global view
(b) Close-up view
Image processing

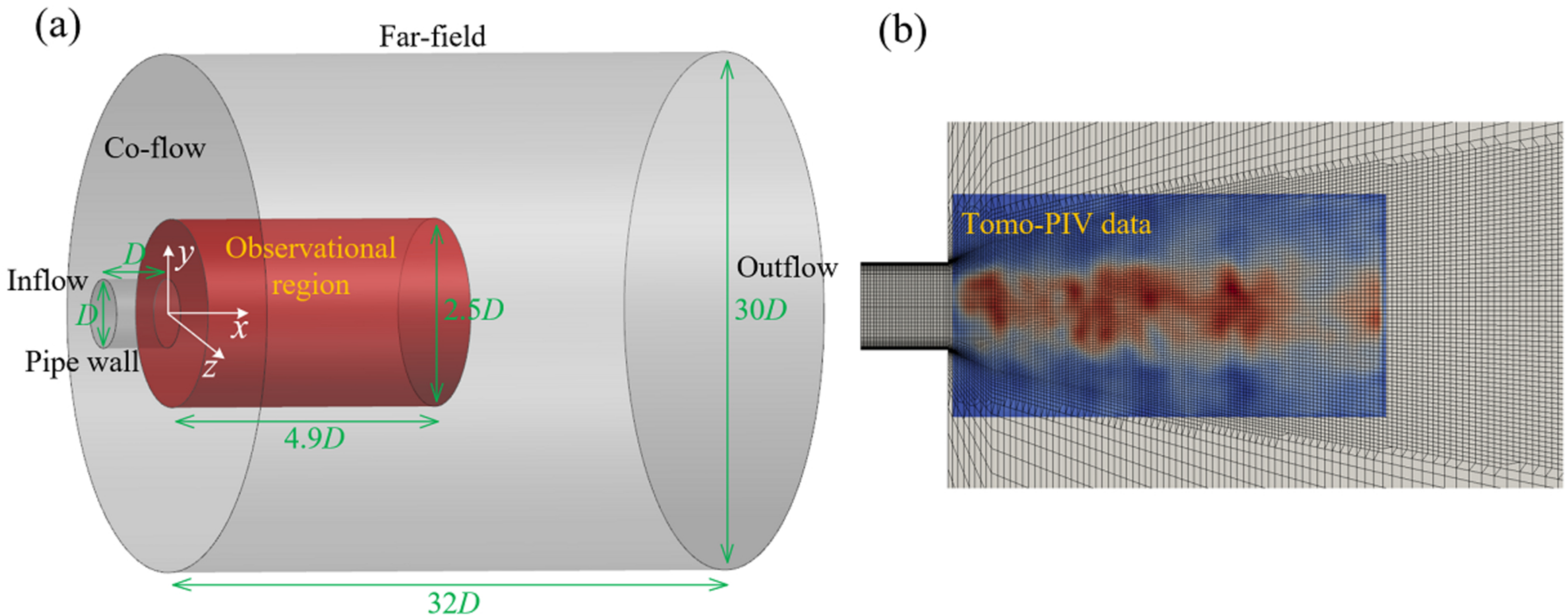
(a)
Far-field
Co-flow
Observational region
D
y
Inflow
D
x
z
Pipe wall
2.5D
Outflow
30D
4.9D
32D
(b)
Tomo-PIV data

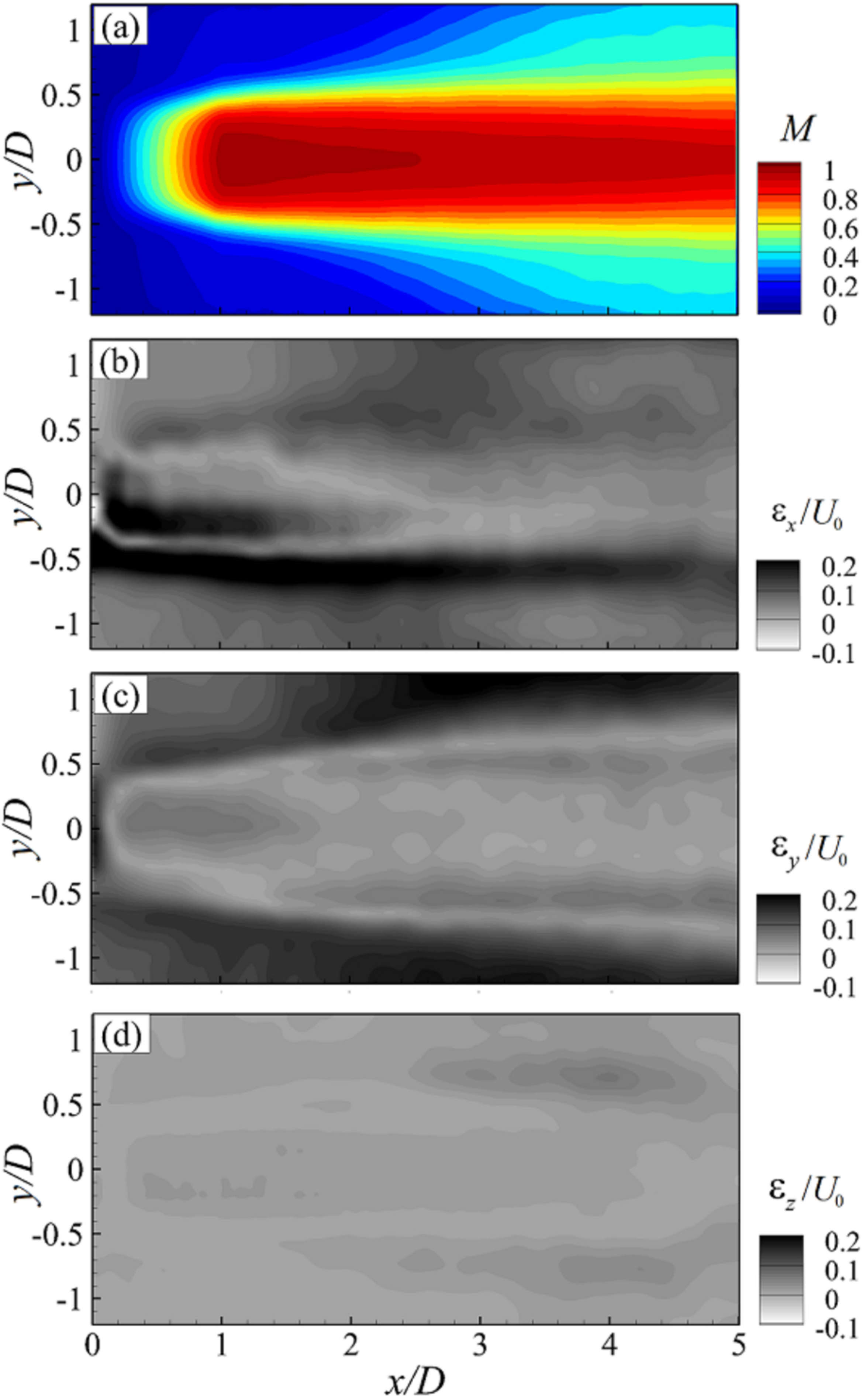
(a)
(b)
(c)
(d)
y/D
1
0.5
0
-0.5
-1
M
1
0.8
0.6
0.4
0.2
0
ε_x/U_0
ε_y/U_0
ε_z/U_0
0.2
0.1
0
-0.1
x/D
0
1
2
3
4
5

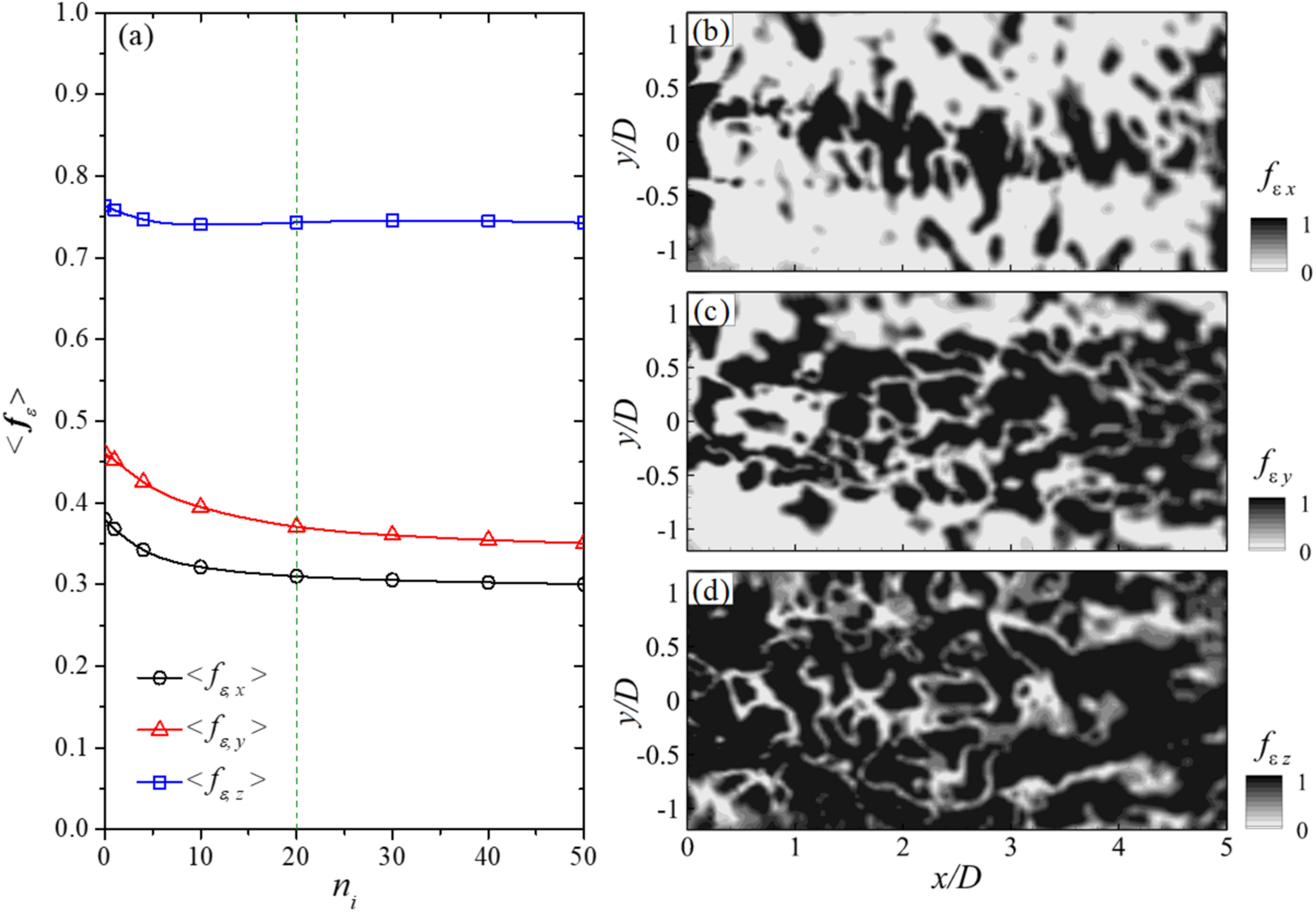
(a)
$<f_\varepsilon>$
n_i
1.0
0.9
0.8
0.7
0.6
0.5
0.4
0.3
0.2
0.1
0.0
0
10
20
30
40
50
$<f_{\varepsilon,x}>$
$<f_{\varepsilon,y}>$
$<f_{\varepsilon,z}>$
(b)
(c)
(d)
y/D
x/D
1
0.5
0
-0.5
-1
2
3
4
5
$f_{\varepsilon x}$
$f_{\varepsilon y}$
$f_{\varepsilon z}$

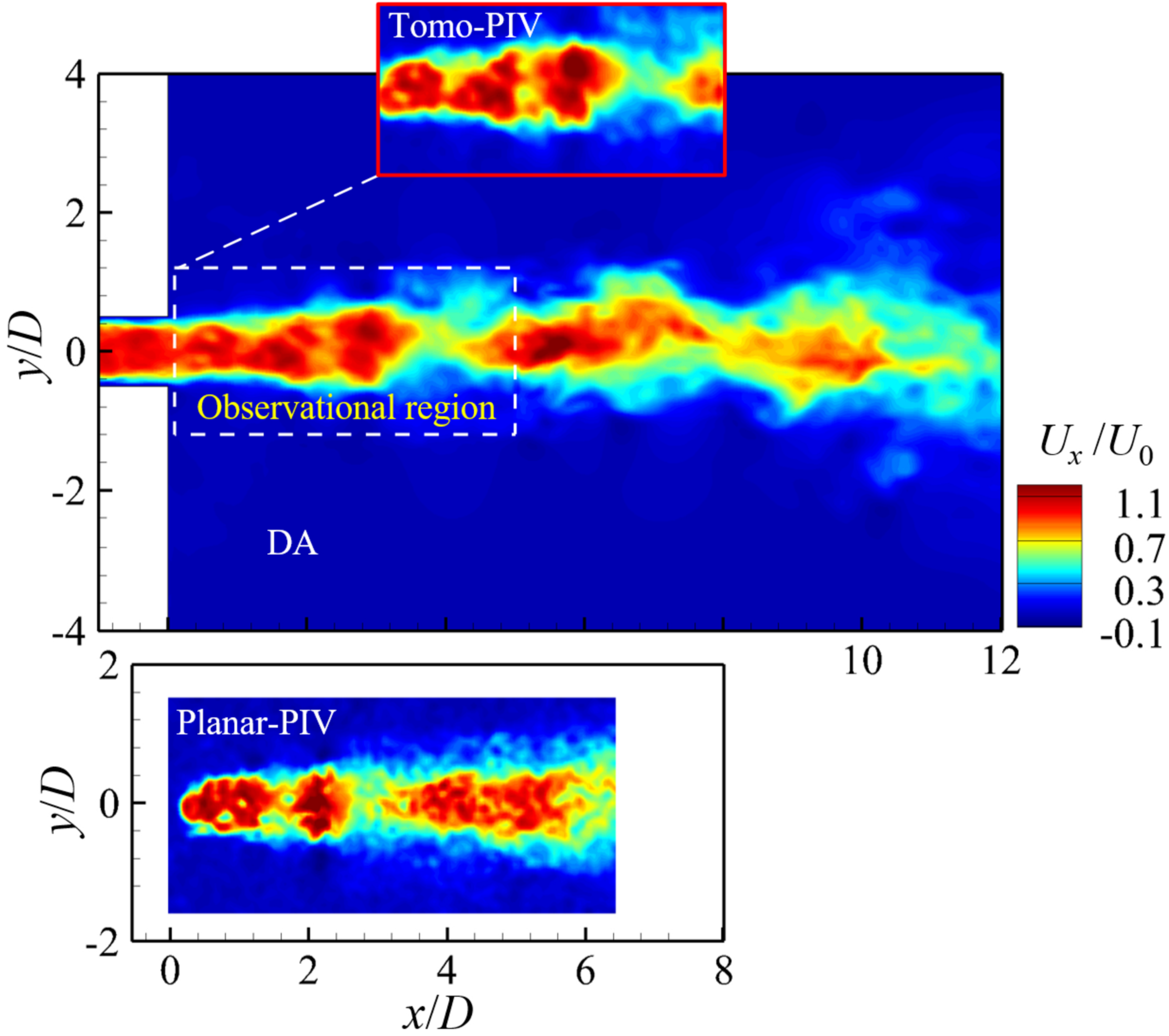
Tomo-PIV
4
2
0
-2
-4
y/D
Observational region
DA
U_x /U_0
1.1
0.7
0.3
-0.1
10
12
2
Planar-PIV
y/D
0
-2
0
2
4
6
8
x/D

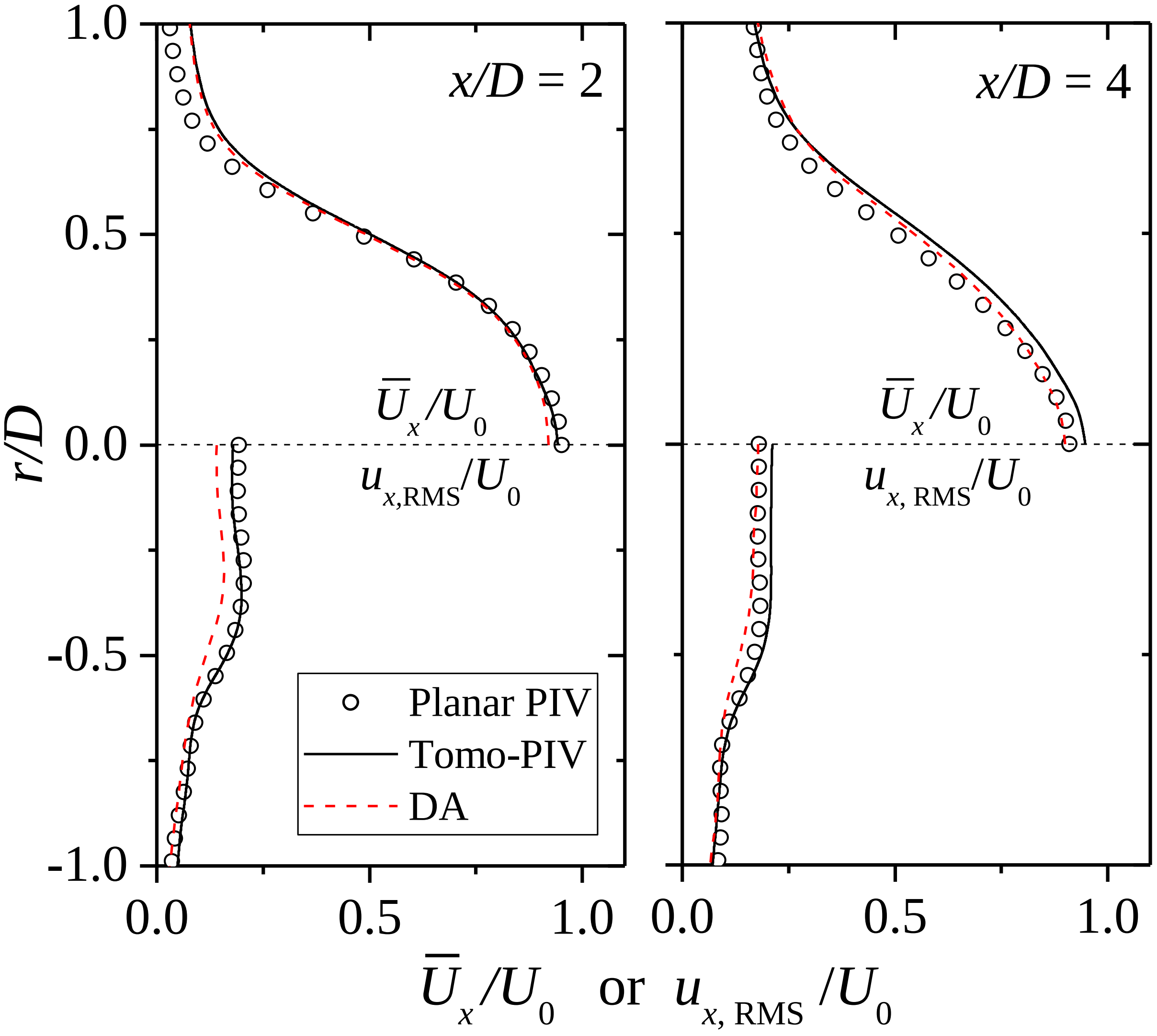

x/D = 2
x/D = 4
$\bar{U}_x/U_0$
$u_{x,\mathrm{RMS}}/U_0$
$\bar{U}_x/U_0$
$u_{x,\,\mathrm{RMS}}/U_0$
Planar PIV
Tomo-PIV
DA
r/D
1.0
0.5
0.0
-0.5
-1.0
0.0
0.5
1.0
0.0
0.5
1.0
$\bar{U}_x/U_0$ or $u_{x,\,\mathrm{RMS}}/U_0$

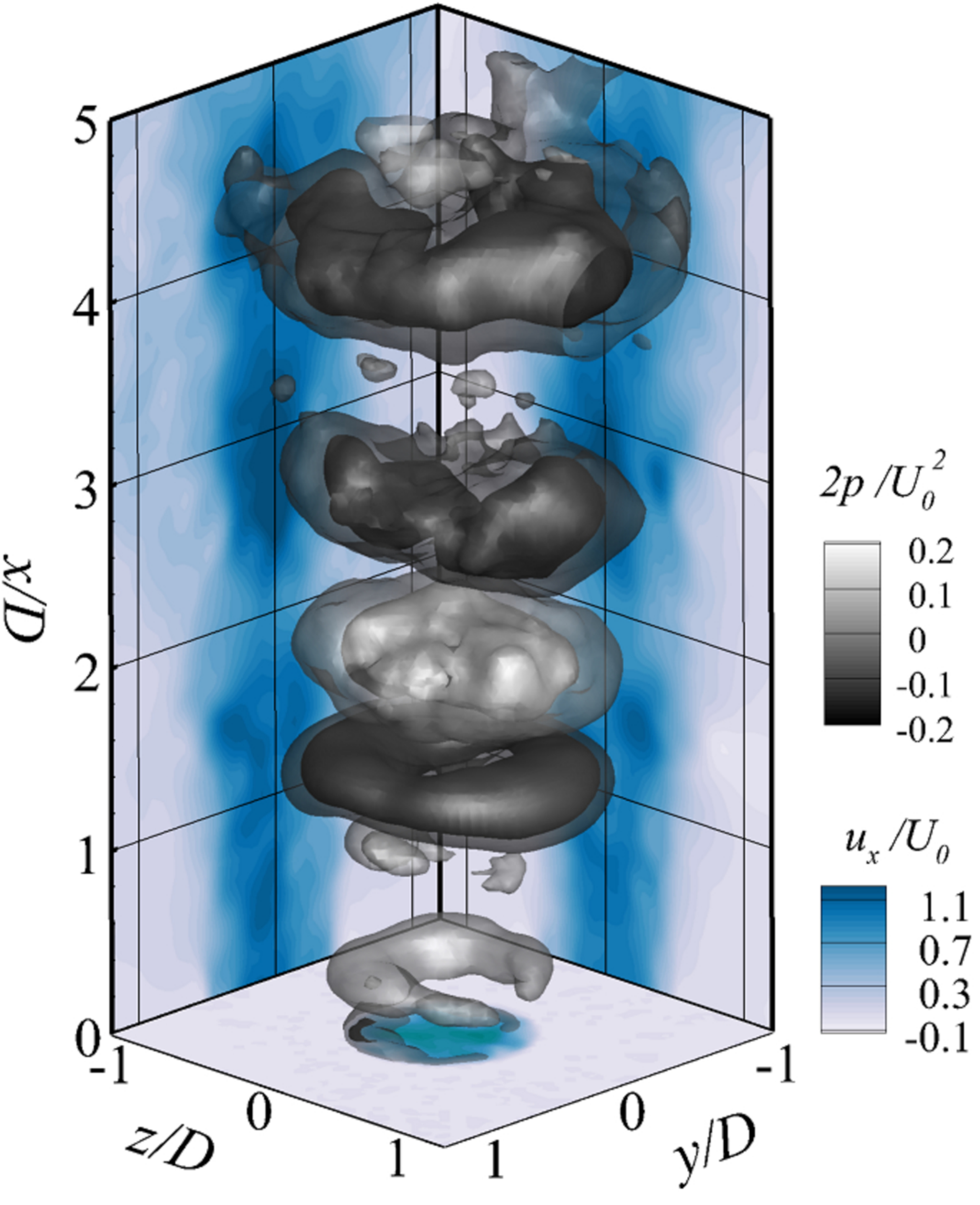
5
4
3
2
1
0
x/D
-1
0
1
z/D
-1
0
1
y/D
$2p/U_0^2$
0.2
0.1
0
-0.1
-0.2
u_x/U_0
1.1
0.7
0.3
-0.1

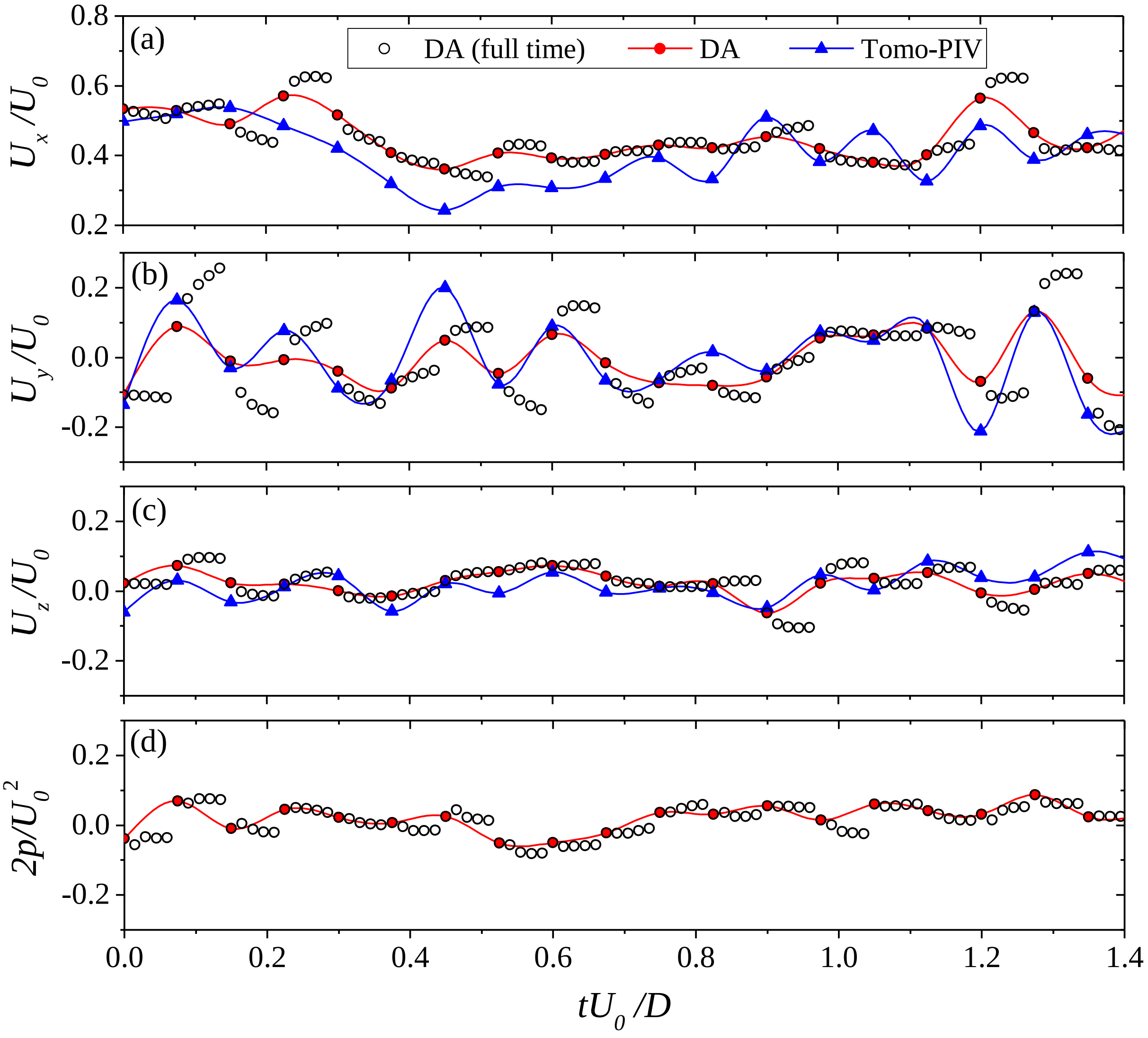
(a)
(b)
(c)
(d)
DA (full time)
DA
Tomo-PIV
U_x/U_0
U_y/U_0
U_z/U_0
$2p/U_0^2$
tU_0/D
0.8
0.6
0.4
0.2
0.2
0.0
-0.2
0.0
0.2
0.4
0.6
0.8
1.0
1.2
1.4

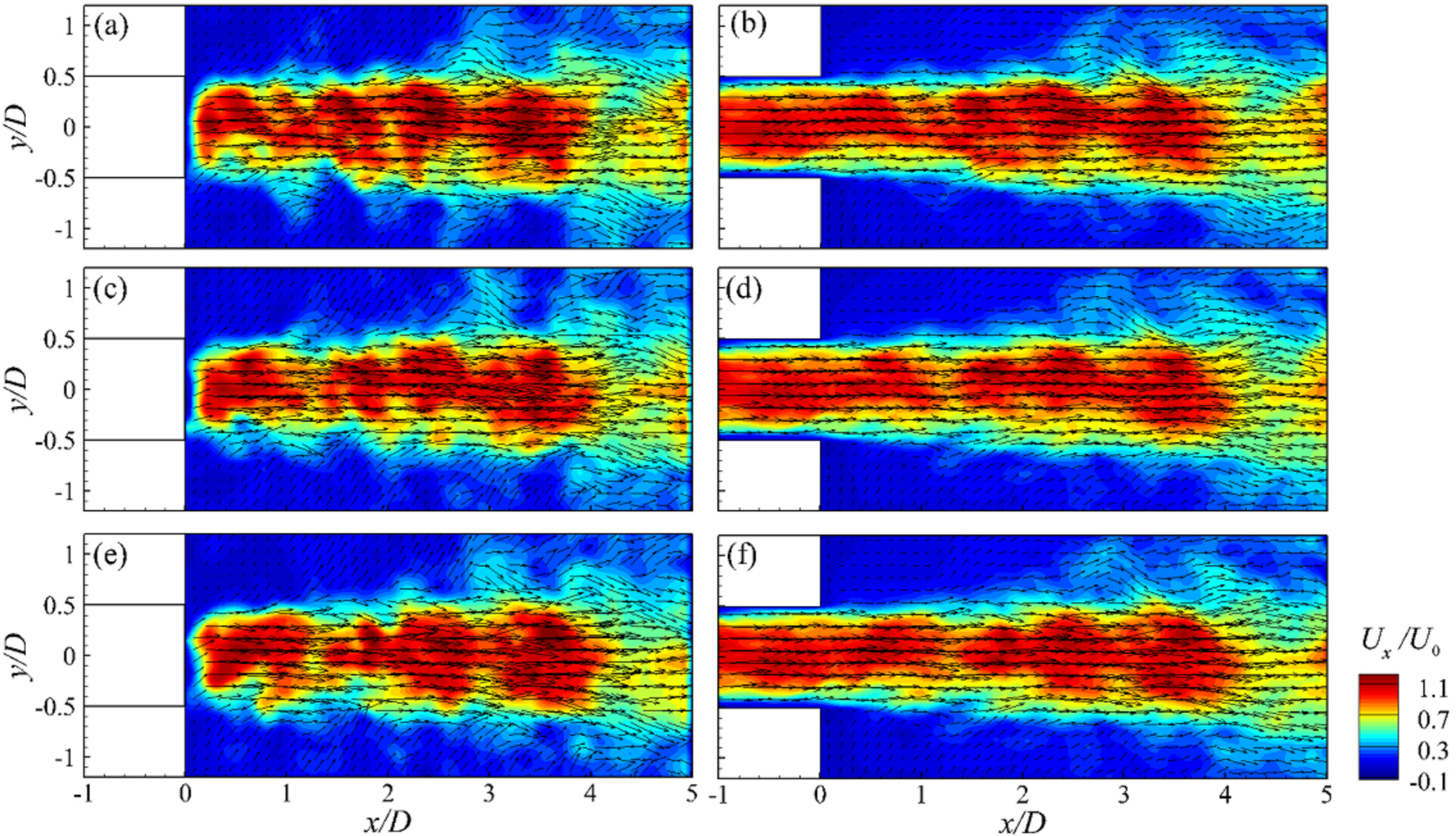
(a)
(b)
(c)
(d)
(e)
(f)
y/D
1
0.5
0
-0.5
-1
x/D
-1
0
1
2
3
4
5
U_x/U_0
1.1
0.7
0.3
-0.1

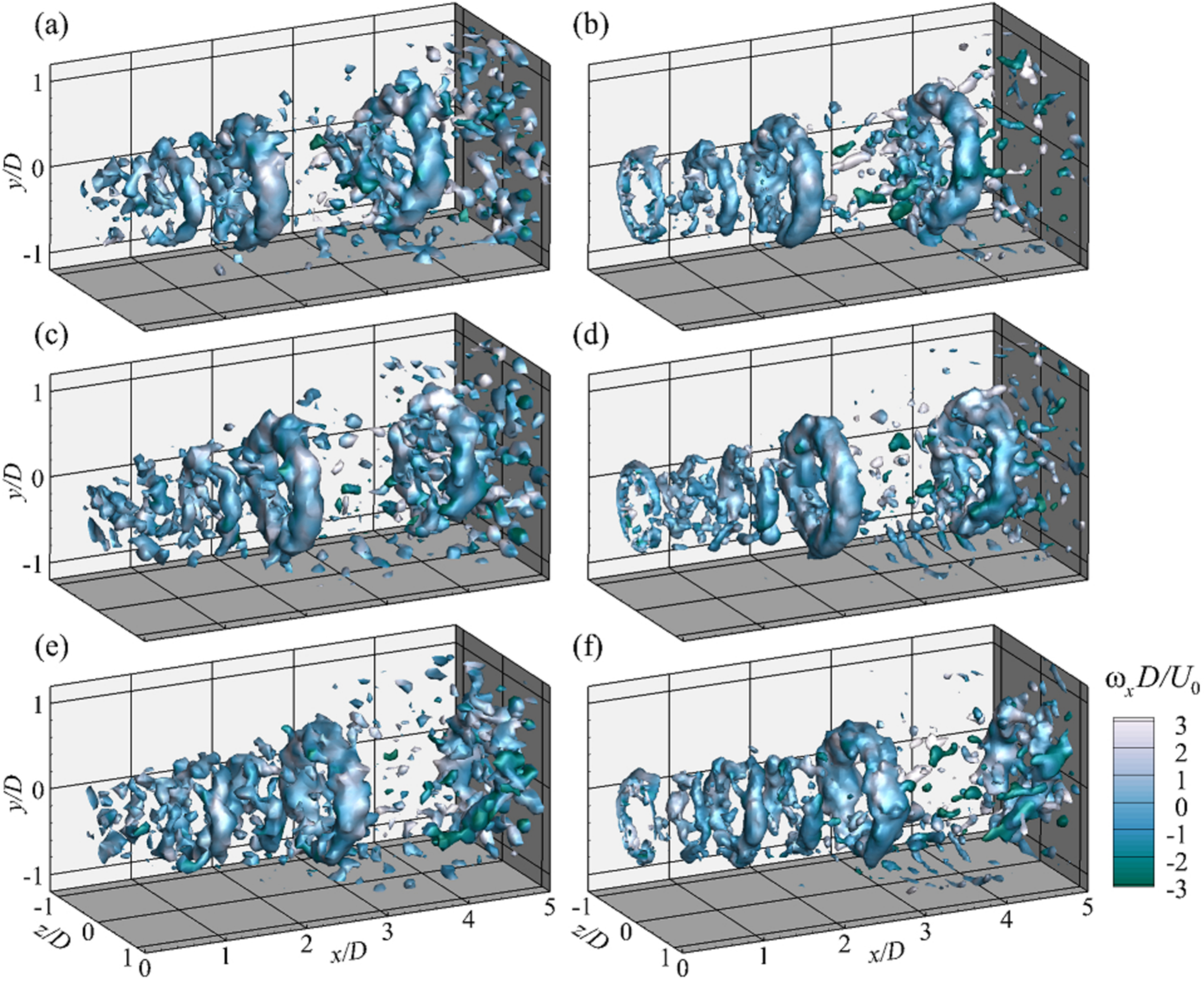
(a)
(b)
(c)
(d)
(e)
(f)
y/D
1
0
-1
z/D
-1
0
1
x/D
0
1
2
3
4
5
ω_x D/U_0
3
2
1
0
-1
-2
-3

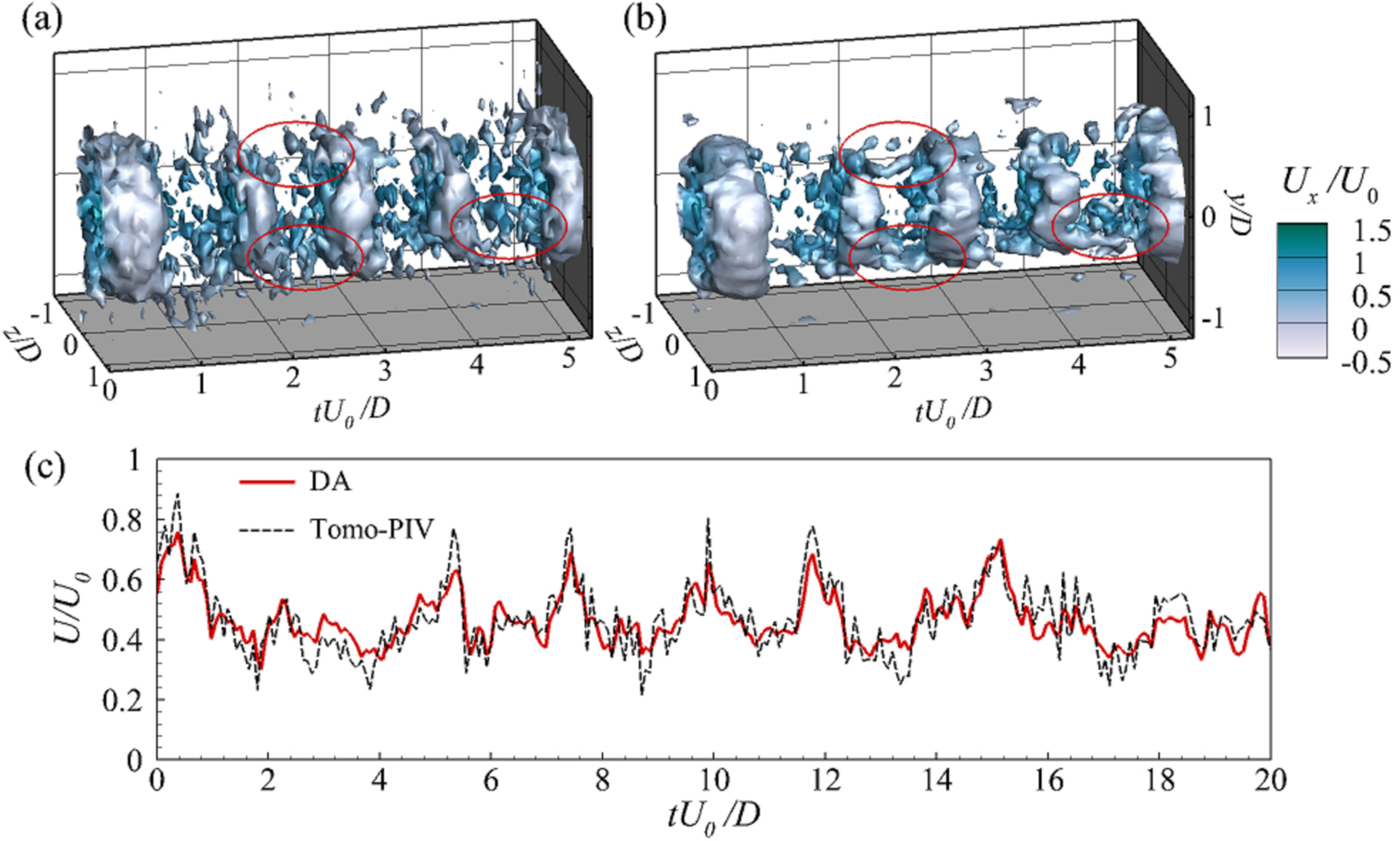
(a)
(b)
U_x/U_0
1.5
1
0.5
0
-0.5
y/D
1
0
-1
z/D
-1
0
1
tU_0/D
0
1
2
3
4
5
(c)
DA
Tomo-PIV
U/U_0
0
0.2
0.4
0.6
0.8
1
tU_0/D
0
2
4
6
8
10
12
14
16
18
20

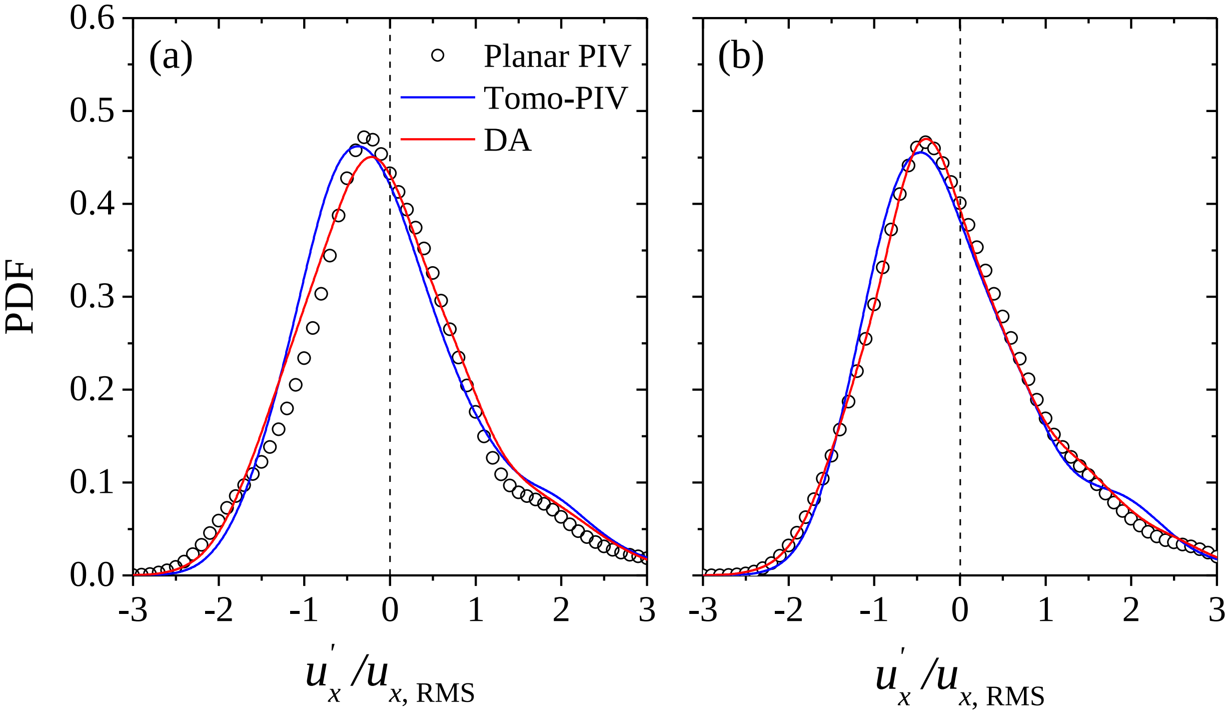
(a)
(b)
Planar PIV
Tomo-PIV
DA
PDF
0.0
0.1
0.2
0.3
0.4
0.5
0.6
-3
-2
-1
0
1
2
3
$u'_x/u_{x,\,\mathrm{RMS}}$
$u'_x/u_{x,\,\mathrm{RMS}}$

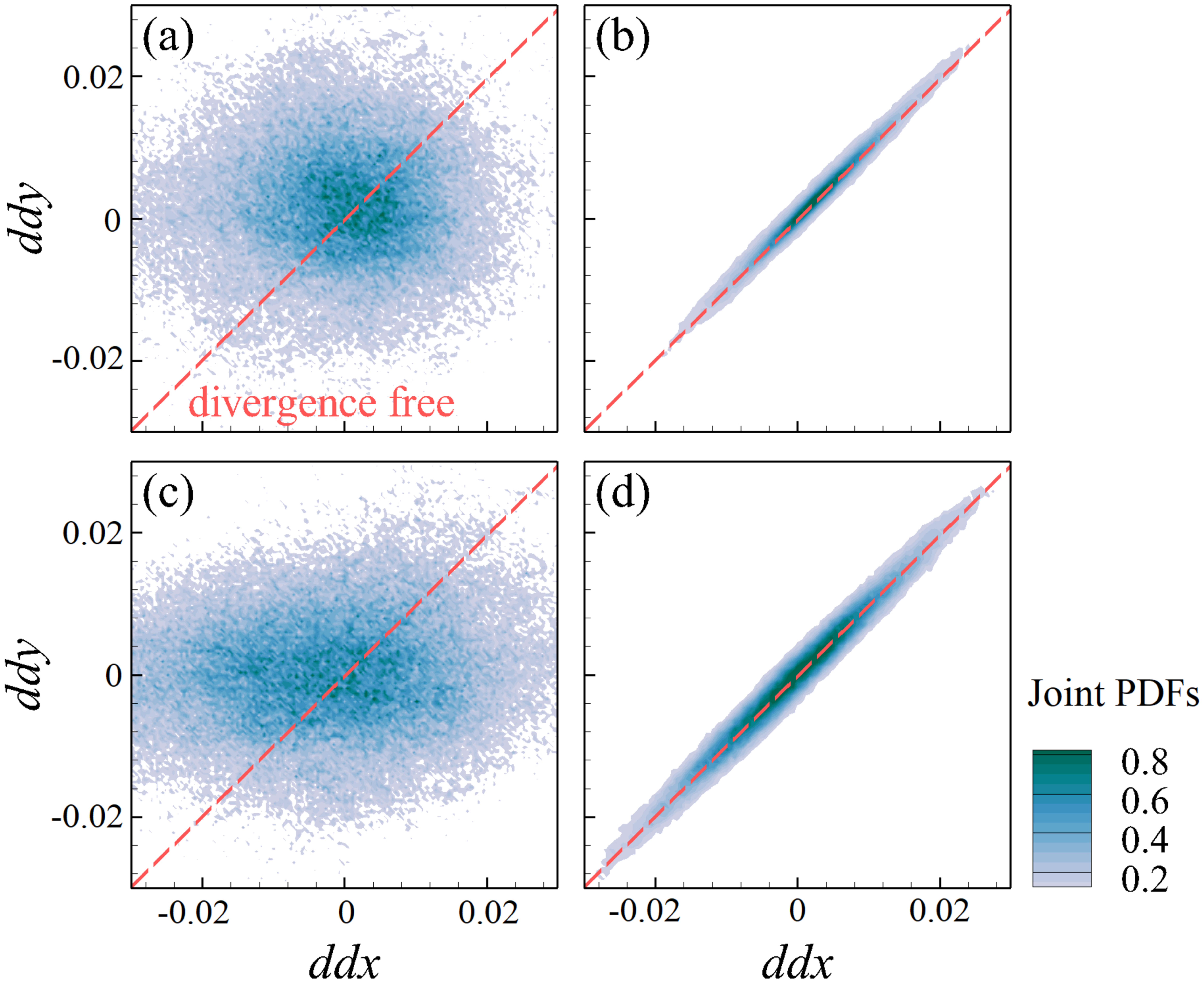
(a)
(b)
(c)
(d)
0.02
0
-0.02
ddy
ddx
-0.02
0
0.02
divergence free
Joint PDFs
0.8
0.6
0.4
0.2

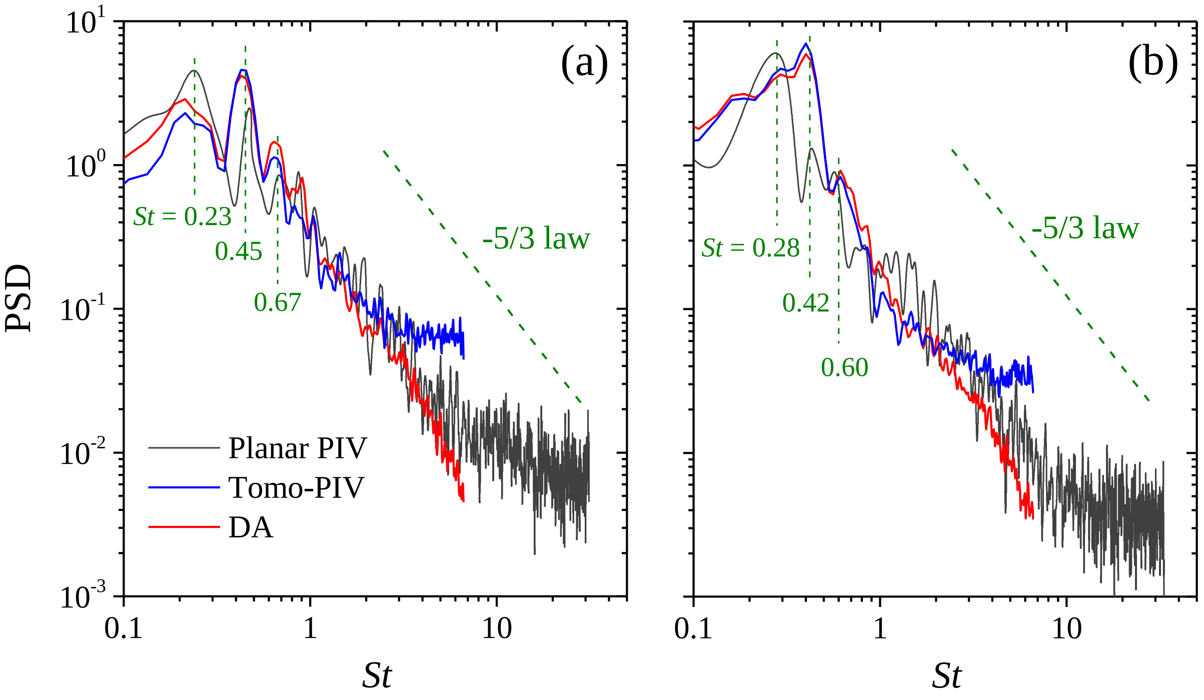

PSD
10^1
10^0
10^{-1}
10^{-2}
10^{-3}
(a)
St = 0.23
0.45
0.67
-5/3 law
Planar PIV
Tomo-PIV
DA
0.1
1
10
St
(b)
St = 0.28
0.42
0.60
-5/3 law
0.1
1
10
St

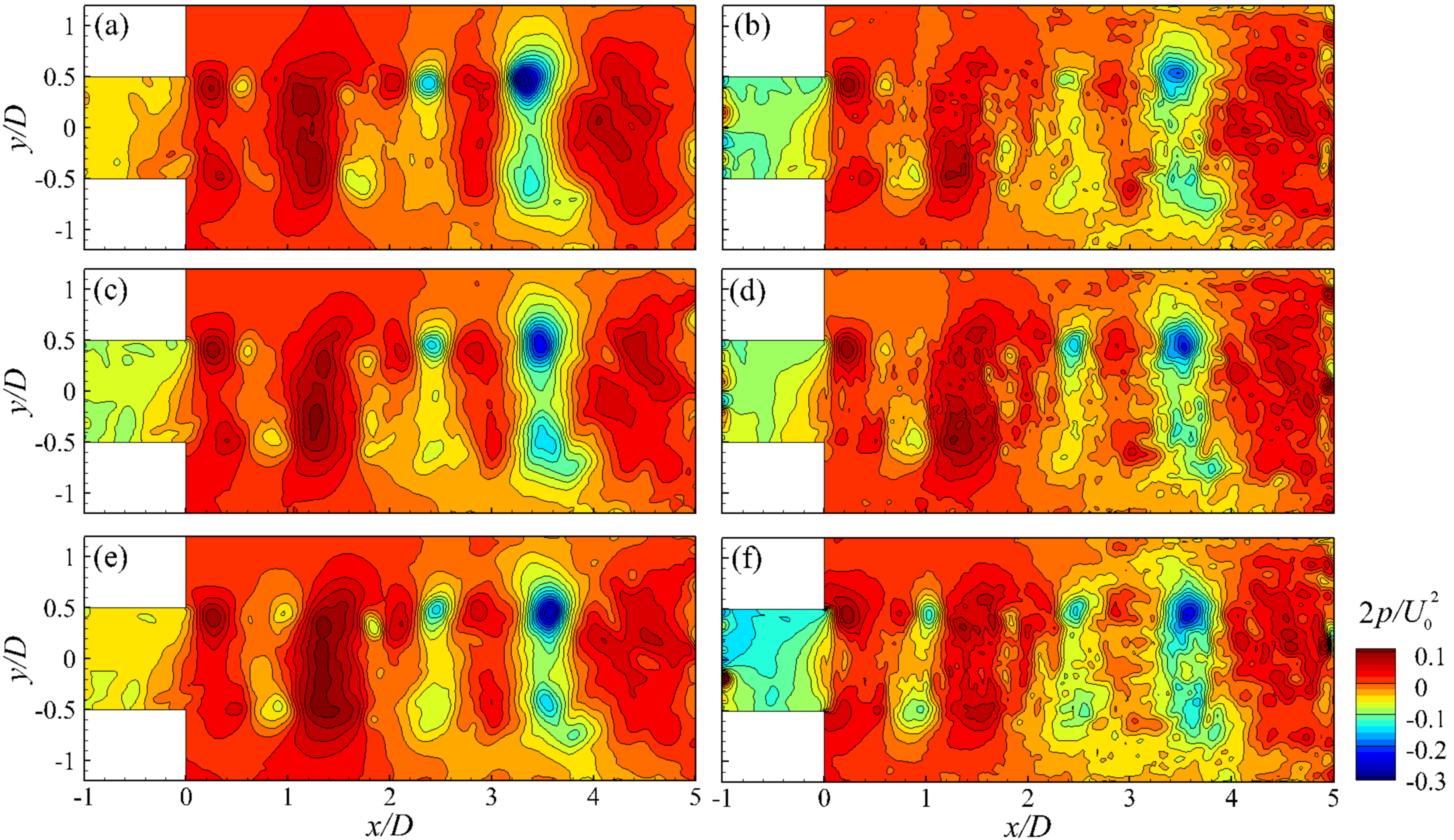
(a)
(b)
(c)
(d)
(e)
(f)
y/D
x/D
1
0.5
0
-0.5
-1
-1
0
1
2
3
4
5
$2p/U_0^2$
0.1
0
-0.1
-0.2
-0.3

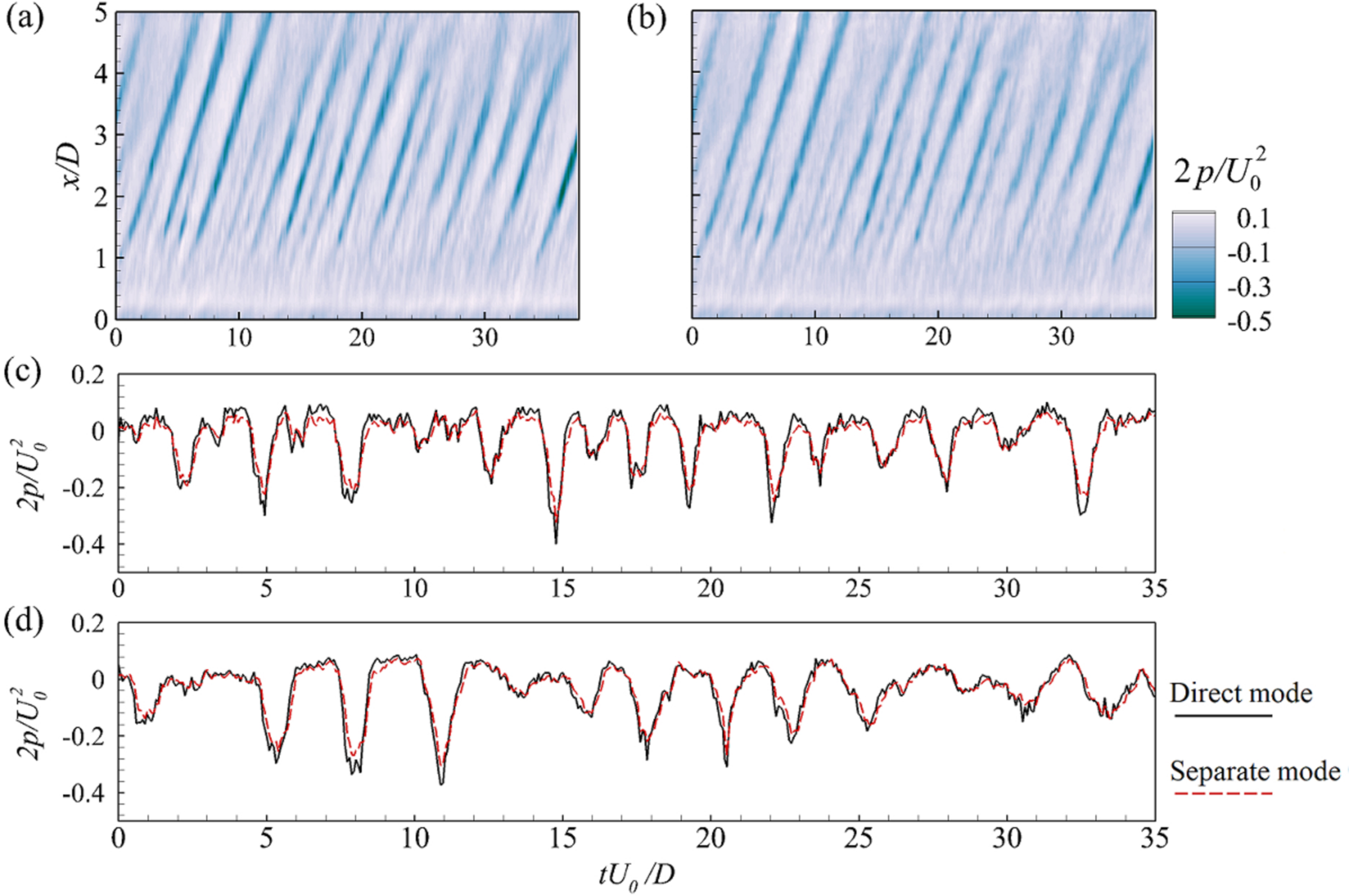
(a)
(b)
x/D
0
1
2
3
4
5
0
10
20
30
2p/U_0^2
0.1
-0.1
-0.3
-0.5
(c)
(d)
0.2
0
-0.2
-0.4
2p/U_0^2
0
5
10
15
20
25
30
35
tU_0/D
Direct mode
Separate mode